






Analysis of flow-wall deformation coupling in high Reynolds number compliant wall boundary layers

Yuhui Lu,¹ Tianrui Xiang¹ , Tamer A. Zaki¹  and Joseph Katz¹ 

¹Department of Mechanical Engineering, Johns Hopkins University, Baltimore, MD 21218, USA

Corresponding author: Joseph Katz, katz@jhu.edu

(Received 5 March 2025; revised 7 July 2025; accepted 12 August 2025)

Interactions of turbulent boundary layers with a compliant surface are investigated experimentally at $Re_\tau = 3300\text{--}8900$. Integrating tomographic particle tracking with Mach–Zehnder interferometry enables simultaneous mapping of the compliant wall deformation and the three-dimensional velocity and pressure fields. Our initial study (*J. Fluid. Mech.* vol. 980, R2) shows that the flow–deformation correlations decrease with increasing Re_τ , despite an order of magnitude increase in deformation amplitude. To elucidate the mechanisms involved, the same velocity, pressure and kinetic energy fields are decomposed to ‘wave-coherent’ and ‘stochastic’ parts using a Hilbert projection method. The phase dependent coherent variables, especially the pressure, are highly correlated with the wave, but decrease with increasing Re_τ . While the coherent energy is 6%–10% of the stochastic level, the pressure root mean square is comparable near the wall. The energy flux between the coherent and stochastic parts and the pressure diffusion reverse sign at the critical layer. To explain the Re_τ dependence, the characteristic deformation wavelength (three times the thickness) is compared with the scales of the energy-containing eddies in the boundary layer represented by the k^{-1} range in the energy spectrum. When the deformation wavelength is matched with the $k_x E_{uu}$ peak at the present lowest Re_τ , the flow–deformation correlations and coherent pressure become strong, even for submicron deformations. In this case, the flow and wall motion become phase locked, suggesting resonant behaviours. As Re_τ increases, the wall wavelengths and spectral range of attached eddies are no longer matched, resulting in reduced correlations and lower coherent energy and pressure, despite larger deformation.

Key words: boundary layer structure, wave-turbulence interactions

1. Introduction

The interactions of compliant surfaces with laminar or turbulent boundary layers have been the subject of theoretical, experimental and numerical research over the past decades. The main research interests have included changes to skin friction, flow–deformation interactions as well as noise suppression. In the present study, we focus on the flow–deformation interactions of a fully developed boundary layer with a viscoelastic compliant wall. The early attempts to study the compliant wall boundary layer date back to Kramer’s (1957, 1962) effort to mimic the dolphin’s skin aimed at potential drag reduction. Despite the numerous studies that have followed, there is no consensus on whether one can reduce drag using a compliant wall. The past studies can be divided to those focusing on compliance effects on laminar boundary layer transition to turbulence, and those investigating turbulent flows. Early studies (Benjamin 1960; Landahl 1962; Lee, Fisher & Schwarz 1995; Wang, Yeo & Khoo 2006) in favour of drag reduction fall in the first category, and suggest that the wall compliance could suppress the Tollmien–Schlichting waves. For turbulent boundary layers, results have been mixed – some report drag reduction (e.g. Fisher & Blick 1966; Choi *et al.* 1997; Fukagata *et al.* 2008), some find negligible effects (e.g. Lissaman & Harris 1969; McMichael, Klebanoff & Mease 1980; Endo & Himeno 2002) and others observe drag increase (Boggs & Hahn 1962). More recent experimental studies using two-dimensional (2-D) particle image velocimetry (PIV) (Wang, Koley & Katz 2020; Greidanus *et al.* 2022) and three-dimensional (3-D) tomographic particle tracking (Lu *et al.* 2024) show an increasing downward shift in the mean velocity profile, indicating drag increase, with increasing deformation magnitude. Recent direct numerical simulation (DNS) by Rosti & Brandt (2017) and Esteghamatian, Katz & Zaki (2022) have also observed the momentum deficit, as well as an increase in near-wall turbulence with decreasing material stiffness, consistent with the experiments.

Several types of wave propagation have been observed on the compliant surface. When the free stream velocity (U_0) is larger than the shear speed of the material ($c_t = \sqrt{G/\rho_s}$, where G and ρ_s are the shear modulus and density), e.g. $U_0/c_t > 2.8$, Gad-El-Hak, Blackwelder & Riley (1984) and Duncan (1986) show that the deformation wave contains a slowly propagating ($\sim 0.05U_0$), high-amplitude, ‘static divergence wave’. This wave is also observed in Greidanus *et al.* (2022) for $U_0/c_t > 3.5$. With increasing material stiffness, the deformation wave consists primarily of ‘travelling-wave flutter’, which travels at a fraction of the free stream velocity (Gad-el-Hak 1986). Data compiled in the review by Carpenter, Davies & Lucey (2000) indicates that the phase speed of this wave varies between $0.4U_0$ to $0.8U_0$, consistent with recent experiments (Zhang *et al.* 2017; Wang *et al.* 2020; Greidanus *et al.* 2022; Lu *et al.* 2024). This phase speed does not show a consistent trend with either hydrodynamic or material parameters, a topic that has not been resolved yet. In addition, Rosti & Brandt (2017) and Wang *et al.* (2020) observe long streamwise deformations resembling boundary layer superstructures (Hutchins & Marusic 2007). Essentially all the recent experimental and computational studies (Rosti & Brandt 2017; Wang *et al.* 2020; Esteghamatian *et al.* 2022; Greidanus *et al.* 2022) report that the wall deformations enhance the near-wall turbulence and Reynolds shear stress, although the observed profiles vary. Wang *et al.* (2020) also observe that the deformations decrease the correlation length scales of streamwise velocity fluctuations, which they attribute to ‘scrambling’ of the eddies by the surface motions.

Studying the dynamic interaction between flow and deformation requires time-resolved measurements of both. Early experiments were limited to single-point flow data and separate deformation mapping (e.g. Gad-El-Hak *et al.* 1984; Lee, Fisher & Schwarz 1993a). Over recent years, techniques such as holography (Lee, Fisher & Schwarz

1993b), laser Doppler vibrometer (Castellini, Martarelli & Tomasini 2006), Mach–Zehnder interferometry (Zhang, Miorini & Katz 2015), background oriented schlieren (Charruault, Greidanus & Westerweel 2018) and digital image correlation (Huynh & McKeon 2020) have been used to measure wall deformation. Zhang *et al.* (2015) and Zhang *et al.* (2017) have performed the first simultaneous measurement, combining tomographic PIV and Mach–Zehnder interferometry (MZI). The pressure field is measured by spatial integration of the material acceleration and correlated with the spatiotemporal distribution of deformation. In their studies, the wall is quite rigid ($c_t = 6.8U_0$), resulting in submicron deformations with heights (d) that are 2–3 orders of magnitude smaller than the wall unit ($\delta_v = \nu/u_\tau$, where ν is the kinematic viscosity and $u_\tau = (\tau_w/\rho)^{1/2}$ is the friction velocity, τ_w is the wall shear stress and ρ is the fluid density). Hence, the interaction mostly involves one-way coupling, i.e. the flow causes wall deformation, but the deformation is too small to have a significant effect on the flow. Conditional sampling shows that surface bumps preferentially reside under pressure minima located between the legs of hairpin vortices, and dimples are associated with pressure maxima at the transition between sweeps and ejections. Subsequent experiments by Wang *et al.* (2020) consist of MZI applications and separate 2-D PIV measurements under conditions of two-way coupling, involving a softer material with d being of the same order as δ_v . In these cases, the velocity deficit in the inner part of the boundary layers starts to appear even for deformations of the order of $0.1\delta_v$. For the same compliant wall, Lu *et al.* (2024) apply tomographic particle tracking to measure the 3-D flow and pressure, and simultaneous MZI for mapping the 2-D wall deformation. This approach is also used for the present study.

Theoretical predictions of linear viscoelastic material response to harmonic excitation have been introduced by Chase (1991) and Benschop *et al.* (2019). Applications of these models by Zhang *et al.* (2017) and Wang *et al.* (2020) lead to the conclusion that the characteristic wavelength of the peak material response is three times the coating thickness (l_0). The experiments by Zhang *et al.* (2017), Wang *et al.* (2020) and Greidanus *et al.* (2022) have confirmed these predictions. For a wide range of material properties ($U_0 < 3.4C_t$), the deformation root mean square (r.m.s.) scaled by l_0 shows a linear relationship with the liquid pressure r.m.s., scaled by the shear modulus (Benschop *et al.* 2019; Greidanus *et al.* 2022; Lu *et al.* 2024), indicating a linear normal stress–strain relationship.

In numerical simulations, a proper model for the compliant material is essential. Recent DNS (Rosti & Brandt 2017; Esteghamatian *et al.* 2022) model the compliant wall as a hyperelastic material and simulate the flow/motion in both media. While Rosti & Brandt (2017) focus on the mean flow profiles and turbulence statistics, Esteghamatian *et al.* (2022) provide detailed accounts of the flow structure. For example, they show the contributions of surface acceleration and pressure gradient on the generation of vorticity. For large deformation, $d \sim 20\delta_v$, the near-wall shear layer detaches at the deformation peak up to a height where the local advection speed is equal to the Rayleigh wave speed. The low momentum fluid on the leeward side is subsequently lifted up by the upward wall motion, and then entrained into the high-speed flow at higher elevations. For small deformation, $d \leq \delta_v$, the experiments of Zhang *et al.* (2017) and Lu *et al.* (2024) show that the pressure–deformation correlation also peaks at an elevation where the local mean velocity is equal to the surface wave speed. Adopting terminology introduced by Miles (1957), and widely used in the air–sea interaction community, Lu *et al.* (2024) refer to this elevation as a ‘critical layer’, and show that it plays an important role in the flow–deformation interactions. For example, the near-wall turbulence is highly correlated and phase-locked with the deformation up to the critical height (y_c), i.e. it has the same advection speed as the deformation wave. At higher elevations, the turbulence is advected with the local mean flow. In these experiments, the critical height increases from

$y_c^+ = 60\text{--}190$ as Re_τ increases from 3300 to 8900. Here, $Re_\tau = u_\tau \delta / \nu$ and $y_c^+ = y_c / \delta_\nu$, where δ is the boundary layer thickness. It should be noted that the phase lock persists at the lowest Re_τ when the characteristic deformation height is of the order of $0.1\delta_\nu$. In contrast to roughness effects, where such small surface perturbations are expected to have a minimal effect on the flow, the turbulence-wave interactions over the compliant wall have significant impact on the near wall dynamics. A plausible explanation for the mechanisms involved is one of the topics of the present paper.

Owing to its significance to the present study, this paragraph provides a brief background on the critical layer and its effect on wind-wave interactions in oceanography. Early efforts to model air-sea interactions date back to Jeffreys' (1925) sheltering hypothesis, which assumes that the symmetric distribution of surface pressure is broken by flow separation on the leeward side, resulting in pressure work on the wave. Phillips (1957) attributes the wave growth to resonant forcing of the surface waves by turbulent pressure fluctuations, while Miles (1957) proposes that an inviscid instability involving a resonance of waves with the airflow occurs at the critical height. Subsequently, Lighthill (1962) further elucidates Miles's theory based on vortex induced forces, leading to the conclusion that the wind-wave energy transfer is concentrated at the critical layer. While Miles's theory has triggered some criticism over the years (e.g. Krasitskii & Zaslavskii 1978; Riley, Donelan & Hui 1982), more recent open-ocean data (e.g. Hristov, Miller & Friehe 2003; Grare, Lenain & Melville 2013) and laboratory experiments (Carpenter, Buckley & Veron 2022) support the important role of the critical layer. As noted above, in Lu *et al.* (2024), we show that for a compliant wall wave, the wave-turbulence correlations peak near the critical height.

In studies of flow-wave interactions, instead of the typical Reynolds decomposition, Hussain & Reynolds (1970) introduce a triple decomposition that separates the flow variables to mean, wave-coherent and background turbulence components. The corresponding decomposed conservation equations for kinetic energy are derived in Reynolds & Hussain (1972), and modified equations for a curvilinear coordinate system have been presented recently by Yousefi & Veron (2020). Separating the wave-coherent motions from the turbulence in experimental data has been a challenge, especially for cases with high background turbulence. Several methods have been utilized, including phase averaging (e.g. Einaudi & Finnigan 1993; Yang & Shen 2010), Hilbert projection (e.g. Hristov, Friehe & Miller 1998; Hristov & Plancarte 2014) and spectral filtering (e.g. Grare *et al.* 2013). Phase averaging is particularly effective when the wave is monochromatic or when only one dominant component is considered, and the latter two methods have been employed when the wave field is broadband, e.g. in field ocean data. In the present study, we use the Hilbert projection to characterize the flow components that are coherent with the wall deformation. In the oceanic boundary layer, the production of wave-coherent kinetic energy is smaller than that of the 'stochastic' background turbulent kinetic energy (Rutgersson & Sullivan 2005; Yousefi, Veron & Buckley 2021) but not negligible. Several studies have shown an energy shift from the wave-coherent motions to the background turbulence (Hsu, Hsu & Street 1981; Makin & Kudryavtsev 1999; Yousefi *et al.* 2021), while others (Rutgersson & Sullivan 2005; Hara & Sullivan 2015) have observed an opposite trend. The present study examines these energy fluxes in the compliant wall boundary layer.

This paper builds upon the introductory analysis in Lu *et al.* (2024), in which we demonstrate the above-mentioned linear pressure-deformation scaling, and the changes to the advection speed of turbulent fluctuations across the critical layer, from the wave speed to the local velocity. Here, we utilize the same three laboratory datasets at $Re_\tau = 3300\text{--}8900$, to investigate the effect of the critical layer on the kinetic energy budget, and

to decompose the unsteady kinetic energy to deformation-wave-coherent and stochastic motions in order to elucidate their interactions.

Furthermore, in an attempt to understand the phase locking between the turbulence and the submicron-scale wall motions, we compare the streamwise scales of wall deformations with those of the ‘attached eddies’ in the boundary layer (Townsend 1976; Perry & Chong 1982; Nickels *et al.* 2005). A brief relevant background on this topic is provided while presenting the data. The experiments involve simultaneous measurements of the time-resolved volumetric flow fields and spatial distribution of wall deformation. The rest of the paper is organized as follows. Descriptions of the flow configuration, experimental set-up and data analysis procedures are summarized in §2. Results of the wave-coherent and stochastic flow variables (velocity, pressure, vorticity, stresses, pressure r.m.s., kinetic energy and their budget terms) are presented in §3. A discussion comparing the deformation wavelength with the length scales of energy-containing eddies in the boundary layer, which is aimed at explaining the Reynolds number scaling of flow–deformation correlations, is provided in §4, followed by conclusions in §5.

2. Experimental set-up and procedures

Throughout the paper, x , y and z are the streamwise, wall-normal and spanwise directions, respectively, and the corresponding velocity components are u , v and w . The free stream velocity, material thickness and critical height are denoted as U_0 , l_0 and y_c , respectively. Here, U_0 is the velocity outside of the boundary layer at the location of measurements, and as demonstrated for a rigid wall in the same facility (Wang *et al.* 2020), the grooves generate a fully developed turbulent boundary layer in the sample area with the typical velocity profile, consisting of viscous, buffer, log and outer layers. Accordingly, U_0 is not expected to change significantly over the sample area. The friction velocity is $u_\tau = \sqrt{\tau_w/\rho}$, where τ_w and ρ are the wall shear stress and the fluid density, the viscous wall unit is $\delta_v = \nu/u_\tau$, where ν is the kinematic viscosity and the friction Reynolds number is $Re_\tau = \delta/\delta_v$, where δ is the boundary layer thickness. Superscript ‘+’ denotes normalization with inner variables, namely by δ_v for length scales, u_τ for velocity, u_τ^2 for Reynolds stresses and ρu_τ^2 for pressure.

The experiments have been performed in the recently constructed Johns Hopkins University refractive index-matched water tunnel, which is sketched in figure 1. This facility is filled with a 62 % by weight aqueous sodium iodide (NaI) solution, which has the same refractive index as acrylic (1.487), but not that of the compliant wall, a kinematic viscosity of $1.1 \times 10^{-6} \text{ m}^2 \text{ s}^{-1}$, and a density of 1850 kg m^{-3} (Bai & Katz 2014). The flow is driven by a 60 HP axial pump whose speed is controlled by an inverter. The top part of this tunnel has been used before in Wang *et al.* (2020) as an extension to another facility, but the pump and the 30.5 cm diameter vertical and lower piping have been constructed recently. The upper section includes a 279.4 cm long, mild inlet diffuser expanding from a 30.5 cm diameter pipe to a rectangular $34.8 \times 40.6 \text{ cm}^2$ settling chamber containing flow straighteners, a nozzle with an area ratio of 4.6 : 1, a test section and an outlet diffuser. The test section, with 50.8 mm thick acrylic windows on all sides (figure 1b), is 83.8 cm long, and has a cross-section of $15.2 \times 20.3 \text{ cm}^2$. A half-filled tank above the test section is connected to sources of compressed gas and a vacuum pump to control the mean pressure in the loop. The tunnel is also equipped with a 0.92 m diameter and 1.52 m high cyclone bubble separator (figure 1c) that can either be connected inline or bypassed using gate valves. The flow enters the cyclone circumferentially at the bottom of the tank and leaves circumferentially at the top of it. The inlet jet velocity is adjustable by restricting the inflow opening using a nozzle. The internal swirl causes bubble migration to the centre

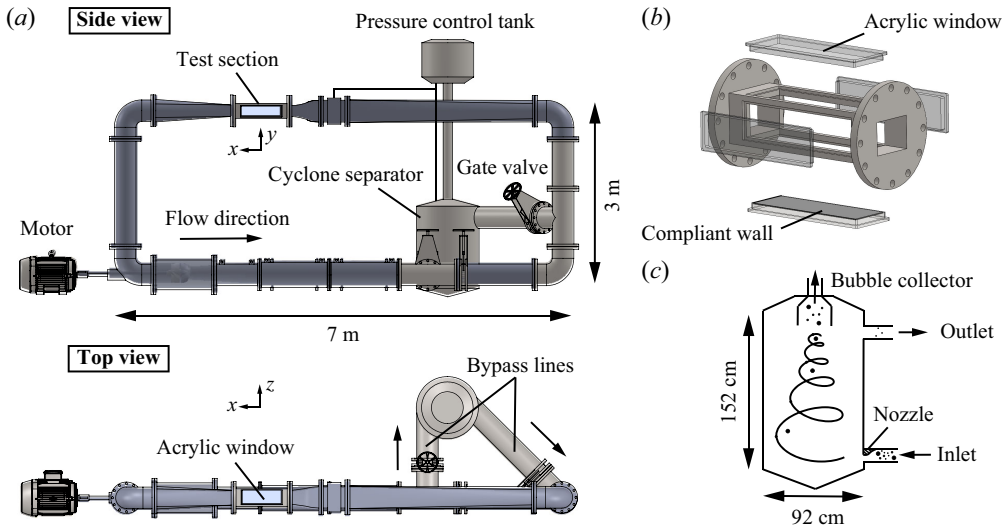


Figure 1. Schematics of (a) the refractive index-matched water tunnel, (b) the test section and (c) the cyclone separator.

of the cyclone, where they are led to the pressure control tank. The cyclone is effective for degassing the water. The current set-up has been shown to remove free stream bubbles larger than $60\text{ }\mu\text{m}$ when the velocities at the entrance to the cyclone is 4.5 m s^{-1} (Lu *et al.* 2021).

Figure 2(a) is a sketch of the compliant wall coating, showing the location of the sample volume. Following Wang *et al.* (2020), the $l_0 = 5\text{ mm}$ thick viscoelastic material is manufactured by mixing polydimethylsiloxane (PDMS, Dow Corning Sylgard 184) with a silicone gel softener (Sylgard 527) at a ratio of 1 : 7.5 by weight. The bottom acrylic tunnel window serves as the moulding base for the coating. Except for a narrow peripheral rim used for securing the coating, the entire bottom window is coated. A chemical primer (Dow Corning Dowsil PR-1204) is applied over the entire area except for the immediate vicinity of the sample area to avoid potential optical distortions. A fresh coating has been used for the present measurements. The present compliant material has a storage modulus (E) of 158 kPa and loss tangent of 0.01. Details on the coating properties and manufacturing procedures are available in Wang *et al.* (2020). Boundary layer trips, consisting of six, 0.5 mm high, triangular tripping grooves are installed immediately downstream of the nozzle to trigger boundary layer transition at the entrance to the test section. The flow and deformation measurements with the compliant wall are carried out 48 cm downstream of the tripping grooves. As demonstrated for a rigid wall (Wang *et al.* 2020), these grooves generate a fully developed turbulent boundary layer at the sample area with the typical velocity profile, consisting of viscous, buffer, log and outer layers. The compliant wall modifies the velocity profiles, causing momentum loss that increases with increasing $E/\rho U_0^2$, as discussed in the introduction.

Figures 2(b) and 2(c) illustrate the optical set-up for simultaneous measurements of the time-resolved 3-D flow field using tomographic particle tracking velocimetry (TPTV), and 2-D wall deformation using MZI. This set-up replicates the approach introduced by Zhang *et al.* (2015), but the velocity measurements are based on tomographic particle tracking instead of tomographic PIV. The experiments have been conducted at three Re_τ ranging from 3300 to 8900. The values of τ_w and δ are determined from a fit to the mean velocity

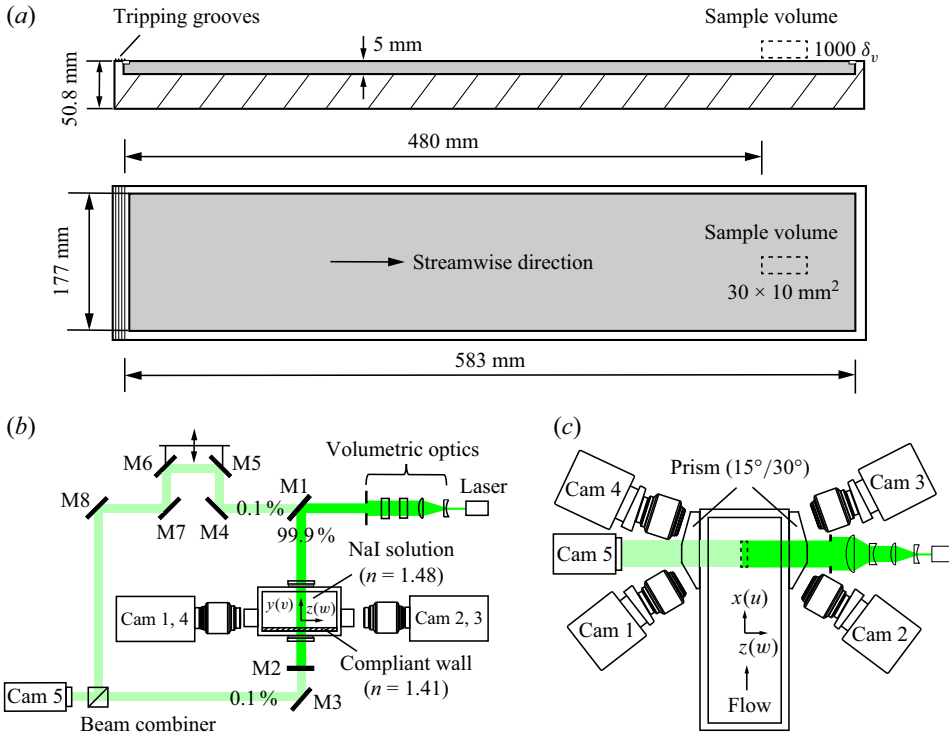


Figure 2. (a) The compliant coating and location of the sample volume, and (b,c) the optical set-up of the integrated TPTV-MZI system shown in (b) front view and (c) top view.

profile in the log layer based on TPTV data and separate stereo-PIV measurements (details follow) that cover the entire boundary layer, respectively. The experimental parameters, such as the sample volume size, field of view, resolution, frame rate and database size (all varying with the Reynolds numbers) are summarized in table 1. The corresponding flow parameters, including $E/\rho U_0^2$, deformation r.m.s. and critical heights, all taken from Lu *et al.* (2024), are also included. Since the optical set-up has been described before in great detail (Zhang *et al.* 2015), it is only summarized here. The 10 mm thick light sheet is generated using a high-speed Nd:YLF laser (Photonics DM60–527), and the flow is seeded with 13 μm diameter silver-coated hollow glass spheres with a specific gravity of 1.6. The corresponding Stokes number is 4.6×10^{-2} , hence these particles are expected to follow the flow (Raffel *et al.* 2018). The test section is located between two backside-polished mirrors (denoted as M1 and M2), which reflect 99.9 % of the light to illuminate the flow field, and the remaining 0.1 % is used for the MZI measurements. The tomographic particle tracking data are recorded by four high-speed cameras (PCO Dimax S4), denoted as Cam 1–4. As the (0.1 %) light transmitted through mirror M2 passes through the compliant wall, its phase is modulated by the surface deformation. The modulated beam is then combined with the reference beam transmitted through M1, and the resulting interference pattern is captured by a fifth high-speed camera (Phantom V2640), marked as Cam 5 in figure 2(b,c). Their optical path lengths are matched by adjusting the reference beam (mirrors M4–M7) until the fringes appear.

Next, we summarize the data processing procedure for the combined TPTV-MZI measurements. In TPTV, the flow field is measured using the ‘shake-the-box’ Lagrangian particle tracking (Schanz, Gesemann & Schröder 2016) available in the Davis 10.2 software.

Re_τ	3300	6700	8900
U_0 (m s ⁻¹)	2.0	4.4	5.8
u_τ (m s ⁻¹)	0.08	0.17	0.22
U_{sw}/U_0	0.53	0.53	0.53
δ (m)	0.045	0.044	0.044
θ (mm)	4.39	4.68	4.73
Re_θ	8200	18 600	25 200
$E/\rho U_0^2$	20.3	4.5	2.5
$d_{rms}^+(d_{peak}^+)$	0.03 (0.22)	0.17 (1.28)	0.44 (3.46)
Deformation skewness	-0.07	-0.16	-0.19
Deformation kurtosis	3.47	3.99	4.09
$y_c^+(y_c/\delta)$	63 (0.019)	165 (0.025)	193 (0.022)
TPTV sample volume $x \times y \times z$	$27 \times 12.8 \times 8.2$ mm ³ ($2000 \times 950 \times 610$ δ_v^3)	$23 \times 8.3 \times 8.2$ mm ³ ($3370 \times 1220 \times 1200$ δ_v^3)	$23 \times 5.5 \times 8.2$ mm ³ ($4540 \times 1090 \times 1620$ δ_v^3)
TPTV camera FOV (PCO dimax S4)	1104×500 pixels	1008×332 pixels	1008×240 pixels
'Binning' interrogation volume in mm and (δ_v)	$0.24 \times 0.24 \times 0.24$ mm ³ ($17.7 \times 17.7 \times 17.7$ δ_v^3)	$0.24 \times 0.24 \times 0.24$ mm ³ ($35.2 \times 35.2 \times 35.2$ δ_v^3)	$0.24 \times 0.24 \times 0.24$ mm ³ ($47.3 \times 47.3 \times 47.3$ δ_v^3)
Interpolated TPTV vector spacing in mm and (δ_v)	0.4 mm (29.6 δ_v)	0.4 mm (58.6 δ_v)	0.4 mm (78.9 δ_v)
MZI field of view $x \times z$	27×10 mm ²	27×10 mm ²	27×10 mm ²
MZI camera FOV (Phantom V2640)	2000×822	2000×822	2000×822
Frame rate (TPTV and MZI)	4545 Hz	6452 Hz	8696 Hz
Recording length	12 909 frames	18 992 frames	26 270 frames

Table 1. The experimental conditions and scales of data acquisition.

The calibration follows the typical two-step procedure involving coarse calibration using a moving target, followed by fine calibrations using the seeded flow field. For the present data, the mean tomographic disparity is approximately 0.05 pixel, with a spatial standard deviation of 0.14 pixel. Data analysis involves tomographic reconstruction, followed by particle tracking, which typically gives approximately 10 000 instantaneous particle tracks. The unstructured velocity and material acceleration are evaluated directly from the particle trajectories, and then interpolated onto a structured grid using constrained cost minimization procedure introduced and analysed by Agarwal *et al.* (2021) and implemented in Agarwal *et al.* (2023). This iterative method minimizes the difference between the interpolated values and the measured one, while constraining the differences between iterations. It also forces the interpolated velocity field to be divergence-free, and the acceleration field, curl-free, while accounting for viscous effects near the wall. The pressure distribution is calculated by spatially integrating the interpolated material acceleration using a 3-D, parallel line, omnidirectional integration method introduced in Wang, Zhang & Katz (2019), and utilized in Zhang *et al.* (2017) and Agarwal *et al.* (2023). To account for viscous effect near the wall, we also include the viscous diffusion terms in the pressure integration as well. The integration procedure also detects paths with significant acceleration errors, based on the local curl, and reduces the weight of these paths. In Agarwal *et al.* (2021), the uncertainty of constrained cost minimization and pressure integration are evaluated using synthetic tracks reproduced from the DNS of turbulent channel flow at $Re_\tau = 1000$ obtained from Johns Hopkins Turbulence database

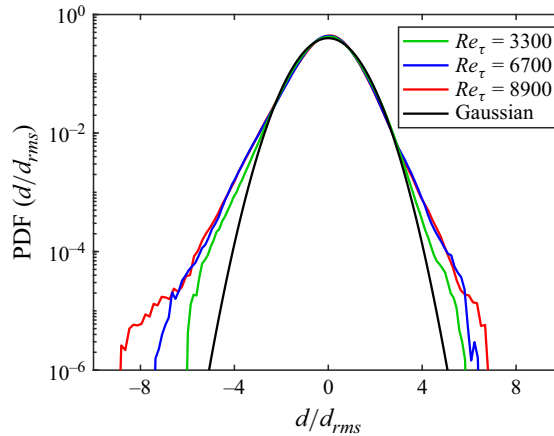


Figure 3. The PDFs of the compliant wall deformations at the indicated Reynolds numbers.

(Graham *et al.* 2016). It shows that the r.m.s. velocity and pressure errors are approximately 3 % and 10 % at $y^+ > 80$, respectively. The velocity error increases to 6 % at lower elevations while the pressure error remains at around 10 %. As discussed in Wang *et al.* (2019) and Agarwal *et al.* (2021), the primary parameter affecting the uncertainty in pressure are the seed particle concentration (scaled by the wall unit), and image acquisition frequency. While the simultaneous flow and wall deformation measurement techniques utilize the same light source, the data acquisition and analysis procedures are totally independent, and do not bias each other (Zhang *et al.* 2015, 2017). Further details about the uncertainty in pressure integration using omnidirectional techniques can be found in Liu & Katz (2006) and Wang *et al.* (2019). To obtain the mean velocity profile from the TPTV data, the calculated particle tracks are projected onto a 2-D plane, and then analysed using a 2-D PIV-based sum-of-correlation method (Meinhart, Wereley & Santiago 2000), using 4×4 pixels ($118 \times 118 \mu\text{m}^2$) interrogation windows. Due to the resolution limit of the TPTV data, the present measurements do not resolve the viscous sublayer and only part of the buffer layer. The first data point for the three Reynolds numbers are located at $y^+ = 30, 59$ and 79 .

The MZI data analysis involves reconstruction of the instantaneous surface shape from the phase distribution of the fringes. Following Zhang *et al.* (2015) and using in-house developed software, the fringes are temporally normalized, and then enhanced using a correlation-based spatial filtering method that generates fringes with uniform amplitudes. The phase distributions are subsequently evaluated from the arc cosine of the enhanced fringes, followed by temporal and spatial unwrapping, as well as detrending. The resulting phase distribution is proportional to the fluctuations in the wall thickness, and to the difference between the refractive index of the NaI solution and that of the compliant material. Calibration tests described in Zhang *et al.* (2015) demonstrate that the deformation height resolution is of the order of 20 nm, ranging between 0.1 % to 0.7 % of the deformation amplitude. The planar spatial resolution of the present deformation measurement, which is defined by the fringe spacing, is $200 \mu\text{m}$. Probability density functions (PDFs) of the compliant wall deformations normalized by their r.m.s. values (available in table 1) for the three Reynolds numbers are presented in figure 3. They demonstrate that in addition to the increase of d_{rms} with increasing Reynolds number, the PDFs deviate further from a Gaussian distribution in the range of infrequent extreme events ($d/d_{rms} > 3$). The comparison with the Gaussian distribution also highlights that the

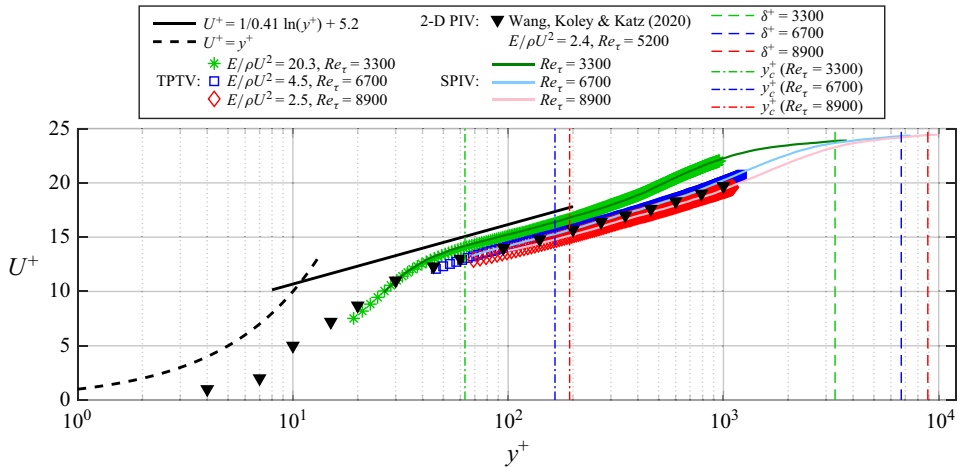


Figure 4. Mean velocity profiles based on the present TPTV (reproduced from Lu *et al.* 2024), stereo PIV and the 2-D PIV data of Wang *et al.* (2020). Dashed lines indicate the boundary layer heights, and dash-dotted lines, the critical heights.

distributions are asymmetric, with more large negative deformations than positive ones. Table 1 also provides information on the skewness and kurtosis of the wall deformation, parameters that have been used for characterizing the effect of rigid roughness on boundary layers (e.g. Flack & Schultz 2014; Busse & Jelly 2023). Consistent with the PDFs in figure 3, the magnitude of wall skewness and the kurtosis increase with Reynolds number. However, they remain rather small, with the skewness varying between -0.07 and -0.19 , and the kurtosis, between 3.5 and 4.1 , i.e. they both do not deviate substantially from those of a Gaussian distribution. These variations are too small for determining the impact of high-order deformation statistics on the wall-deformation coupling.

Since the TPTV field of view (FOV) does not cover the entire boundary layer, to measure its thickness, we have also performed complementing stereo-PIV measurements with a sample area of $30 \times 48 \text{ cm}^2$ at the same location as the TPTV experiments. The images are recorded using two of the high-speed cameras (PCO Dimax S4), fitted with Nikon 105 mm lens, one at each side of the tunnel. The image size is 1100×1870 pixels, and the spatial resolution is $38 \mu\text{m pixel}^{-1}$. While the resolution of these measurements is of the same order as that of the TPTV data, the vertical extent of the FOV covers the entire boundary layers, allowing us to determine δ . The mean velocity profiles are obtained using 4×4 pixels sum-of-correlation available in the Davis 10.2 package, which determines the displacement from the ensemble-averaged cross-correlation. Figure 4 includes the mean velocity profiles from the stereo PIV measurements scaled with inner variables, showing that they resolve the outer part of the log layer and the outer layer. Determining δ from the point where $U/U_0 = 0.99$, and u_τ from a fit to the velocity profile in the log layer, gives the values listed in table 1, along with the three Re_τ of the present experiments, namely $\delta^+ = 3300, 6700$ and 8900 , as indicated also in figure 4. Table 1 also provides the momentum thickness, θ , and the corresponding Re_θ , showing that θ is around $1/10$ of δ , and increases slightly with Reynolds number. Figure 4 also contains the mean streamwise velocity profiles obtained from the present TPTV measurements, and the 2-D PIV data from Wang *et al.* (2020), both reproduced from Lu *et al.* (2024). As is evident, with decreasing $E/\rho U_0^2$, there is a growing deficit in the mean velocity in the log and buffer layers. The 2-D PIV data at $E/\rho U_0^2 = 2.4$, which is obtained for the same compliant wall, and in the same test section, indicate that the velocity deficit extends to the viscous

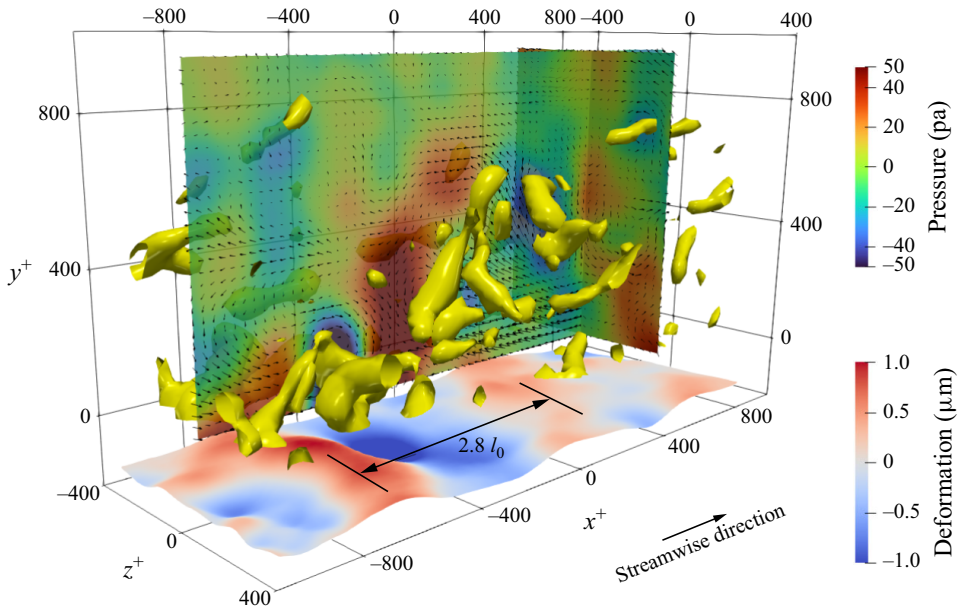


Figure 5. An instantaneous sample snapshot at $Re_\tau = 3300$ of the velocity vectors and pressure contours in two planes, along with the wall deformations presented in exaggerated scales. The 3-D blobs are isosurfaces of $\lambda_2^+ = -1.4 \times 10^{-3}$.

sublayer as well. Similar general behaviour, but with varying extents, are also reported in other experiments (Greidanus *et al.* 2022) and DNS (Rosti & Brandt 2017; Esteghamatian *et al.* 2022).

One should note that the drag increase (i.e. the downward shift of mean velocity profiles in figure 4) rests on the determination of u_τ based on a log-law fit. This method is widely used in experimental studies (e.g. Fernholz & Finley 1996; De Graaff & Eaton 2000), and its limitation has also been discussed extensively (e.g. George & Castillo 1997; Wei, Schmidt & Mcmurtry 2005; Kumar & Mahesh 2022). For example, the bias in log-law fit estimated from channel flow DNS data and pipe flow experimental data are less than 4.3 % and 8 %, respectively (Wei *et al.* 2005). For a smooth rigid wall in the same facility as the present experiments, the high-resolution 2-D PIV measurements by Wang *et al.* (2020) demonstrate a good agreement with the values of u_τ obtained from a log fit and velocity gradients in the viscous sublayer, with discrepancies decreasing from 5.4 % to 1.8 % with increasing Reynolds number. For a compliant wall, in addition to the velocity gradients, one has to account for the non-zero Reynolds shear stress and unsteady form drag (e.g. Rosti & Brandt 2017; Wang *et al.* 2020; Esteghamatian, Zaki & Katz 2022; Greidanus *et al.* 2022). Greidanus *et al.* (2022) compare the wall shear stress in compliant wall boundary layers estimated from a log fit with calculations based on force measurement on a large plate containing the compliant surface. They show a discrepancy of less than 4.7 % between the two methods, confirming that the log fit is a reliable approach when other techniques are not available.

Figure 5 shows a sample instantaneous snapshot of the integrated TPTV/MZI data at $Re_\tau = 3300$. The wavy surface at the bottom shows the instantaneous wall shape with its submicron amplitude variations exaggerated for clarity. Based on statistical analysis of the surface shape (Lu *et al.* 2024), the dominant wavelength of the surface wave is $2.8l_0$, close to the prediction of the Chase (1991) linear model of the surface response

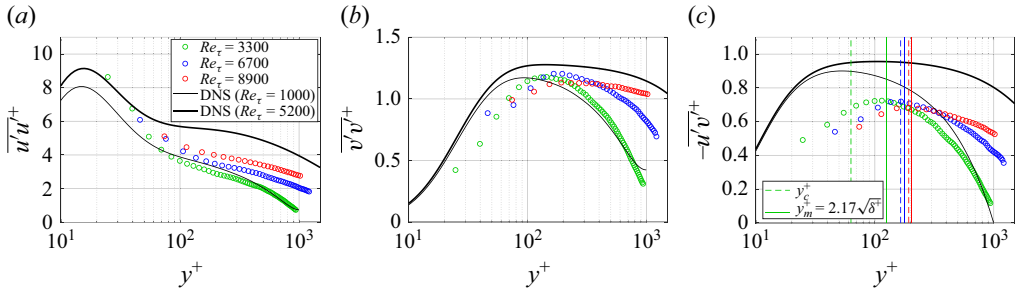


Figure 6. Wall normal profiles of Reynolds stresses: (a) $\overline{u'u'}^+$, (b) $\overline{v'v'}^+$ and (c) $-\overline{u'v'}^+$ non-dimensionalized using inner scaling and compared with results of DNS for rigid smooth walls (solid lines).

to harmonic excitation ($3l_0$). The vectors in the two selected (x, y) and (y, z) planes represent the velocity fluctuations (u', v', w'). The in-plane colour contours indicate the distribution of the pressure fluctuations, and the 3-D blobs representing vortical structures show isosurfaces of $\lambda_2^+ = -1.4 \times 10^{-3}$ (Jeong & Hussain 1995). In this snapshot, the deformation peak appears to be aligned with a pressure minimum, and the trough, with a maximum, consistent with results of conditional analysis described in Lu *et al.* (2024). They also show that the pressure-deformation correlations peak near the critical heights whose elevations are listed in table 1, and indicated as dash-dotted lines in figure 4. Supplemental movies in Lu *et al.* (2024) demonstrate that the large-scale pressure features appear to be phase locked with the deformation and travel with it. The flow and pressure phenomena that appear to travel with the deformation extend to several hundred wall units despite the less than $1 \mu\text{m}$ ($\sim 0.18\delta_v$) deformation height. In the present sample, the pressure minimum above the surface bump appears to be associated with a vortical structure, also consistent with the results of conditional sampling.

3. Results

3.1. Reynolds stresses

Figure 6 presents the wall normal profiles of Reynolds stresses, $\overline{u'u'}$, $\overline{v'v'}$ and $-\overline{u'v'}$, and compares them with DNS data obtained for smooth-wall rigid wall channel flow at $Re_\tau = 1000$ (Graham *et al.* 2016) and $Re_\tau = 5200$ (Lee & Moser 2015), both of them obtained from the Johns Hopkins Turbulence Database (Li *et al.* 2008). Here, the prime indicates the fluctuation from mean value and the overbar refers to ensemble averaging. The present Reynolds stresses are calculated based on spatial ‘binning’ of the particle tracking data, using tools available in the Davis 10.2 software, with $8 \times 8 \times 8$ voxel windows ($0.24 \times 0.24 \times 0.24 \text{ mm}^3$). The corresponding window size in terms of wall units are presented in table 1. This method first calculates the mean velocity using all the tracks in the interrogation volume, and then subtract the mean from each track, followed by ensemble averaging to obtain the Reynolds stresses. The contribution of each track is also weighted by its distance from the interrogation volume centre using a Gaussian weighting function. Consequently, the stresses are under-resolved, especially close to the wall. In the outer part of the boundary layer, the present distribution of $\overline{u'u'}^+$ and $\overline{v'v'}^+$ increase with Reynolds number in the outer layer, as expected, and mostly fall between the two DNS datasets. The profiles of both components collapse as the wall is approached, also consistent with the smooth wall data. However, the present increase in $\overline{u'u'}^+$, and the decrease in $\overline{v'v'}^+$ with decreasing y^+ appear to be faster than those of the smooth wall. In figure 6(c), the three

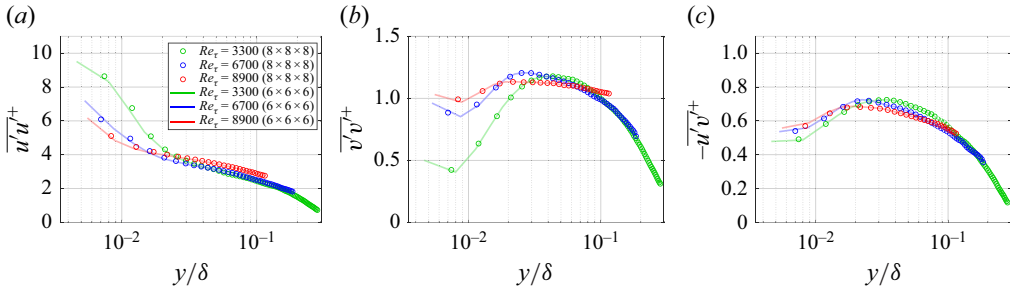


Figure 7. Wall normal profiles of Reynolds stresses plotted using mixed scaling: (a) $\overline{u'u'}^+$, (b) $\overline{v'v'}^+$, (c) $-\overline{u'v'}^+$. Circles, $8 \times 8 \times 8$ voxels binning; lines, $6 \times 6 \times 6$ voxel binning.

profiles of $-\overline{u'v'}^+$ peak in the log layer, but their magnitudes are considerably lower than those of the rigid wall DNS. As discussed in Wang *et al.* (2020) based on comparisons of 2-D PIV data obtained for rigid and compliant walls, the spatial extent of $u'u'$ and $v'v'$, two-point correlations over the compliant wall are substantially lower than those of the smooth wall. This finding implies that the interaction with the compliant material ‘scrambles’ the turbulence, reducing the correlation between the two velocity components, hence the Reynolds shear stress. Yet, figure 6(c) shows that the locations of shear stress peaks are consistent with the empirical relationship obtained for smooth wall boundary layers, $y_m^+ = 2.17\sqrt{\delta^+}$, by Morill-Winter, Philip & Klewicki (2017). Interestingly, y_m^+ is quite close to the critical height, y_c^+ , at $Re_\tau = 6700$ and 8900 , but is nearly twice of y_c^+ at $Re_\tau = 3300$.

Figure 7 demonstrates that trends are different when the same results are plotted using mixed scaling, following Schultz & Flack (2013), i.e. the Reynolds stresses are scaled with u_τ^2 , and y with δ . Replotting the data with y scaled with y_c (not shown) is not significantly different since y_c/δ remains nearly a constant in our measurements (table 1, Lu *et al.* 2024). To assess the effect of the limited spatial resolution, these plots also compare the results obtained for binning volumes of $8 \times 8 \times 8$ voxels with those obtained using $6 \times 6 \times 6$ voxels. As is evident, trends with elevations remain similar, and that increasing resolution increases $\overline{u'u'}^+$ and $\overline{v'v'}^+$ by 10%–20% at low elevations and overlap in the outer layer, while $-\overline{u'v'}^+$ is affected by less than 4%. Both normal stresses nearly collapse in the outer layer, and deviate below the log layer, where $\overline{u'u'}^+$ increases and $\overline{v'v'}^+$ decreases with decreasing Re_τ . The mixed scaling seems to nearly collapse the $-\overline{u'v'}^+$ profiles (figure 7c). These trends, but not the magnitudes, are consistent with those of smooth wall data (DeGraaf & Eaton 2000; Hultmark *et al.* 2012; Schultz & Flack 2013).

We have also tried to compare the present profiles with those presented in Wang *et al.* (2020) and Greidanus *et al.* (2022) for compliant wall boundary layers. In both cases, results do not agree (not shown here). The Greidanus *et al.* (2022) data corresponds to at least an order of magnitude lower $E/\rho U_0^2$, but Re_τ on the 5800–8000 range, and their spatial resolution is lower than the present levels. The Wang *et al.* (2020) stresses are calculated based on standard 2-D PIV measurements at a similar spatial resolution, speeds and wall properties. In mixed scale plots (not shown), trends of $\overline{u'u'}^+$ are similar to the present data, but the present magnitudes are slightly higher. The trends of $\overline{v'v'}^+$ and $-\overline{u'v'}^+$ with increasing Re_τ do not agree, especially their observed sharp increase in stresses near the wall at high Re_τ .

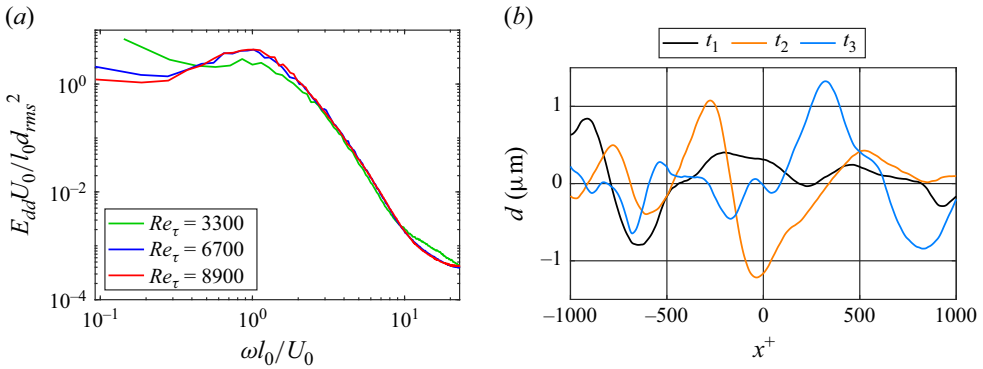


Figure 8. (a) Power spectral densities of the wall deformation, and (b) sample time segments of the instantaneous wall deformation at the indicated times, $z^+ = 0$, and $Re_\tau = 3300$.

3.2. Decomposition of the wave-coherent motion and stochastic turbulence

The velocity and pressure fluctuations in a boundary layer over travelling waves originate either from the shear-driven turbulence or from wave-correlated motions. The wavenumber-frequency spectral analyses in Lu *et al.* (2024) have shown that turbulence is advected with the deformation wave below the critical layer, but follow the mean flow at higher elevations. Furthermore, at all three Reynolds numbers, the flow–deformation coherence peaks at the critical height. To understand the flow–deformation interactions, we would like to examine the characteristic turbulent flow phenomena that propagate with the deformation. Hence, the unsteady flow is decomposed into a wave-coherent part that presumably travels with the wave, and a ‘stochastic’ turbulent part that is not correlated with the wave. To this end, we adopt the ‘triple decomposition’ approach introduced by Hussain & Reynolds (1970) and the Hilbert projection method introduced by Hristov *et al.* (1998), as described briefly here. Each flow variable f is decomposed into its mean \bar{f} (ensemble averaged value), and fluctuating/unsteady part, f' . The latter is further decomposed into a wave-coherent, \tilde{f} , and stochastic (incoherent), f'' , parts, i.e.

$$f = \bar{f} + f' = \bar{f} + \tilde{f} + f''. \quad (3.1)$$

The Hilbert projection method used for determining \tilde{f} , is particularly suitable for data that does not have a dominant periodic frequency or wavelength. A detailed summary of the procedure is provided in the Appendix. The reason that one cannot rely on simple phase averaging is discussed next. Figure 8(a) presents the power spectral densities of the wall deformation, E_{dd} , at the present three Reynolds numbers. They are calculated using fast Fourier transform with a Hanning window available in MATLAB for every point on the surface, and then spatially averaged. The angular frequency ω in rad^{-1} is normalized by U_0/l_0 , and E_{dd} by $l_0 d_{rms}^2/U_0$, where d_{rms} is the r.m.s. of the wall deformation, presented in table 1. Clearly, the three deformation waves have broad ranges of frequencies, all peaking at a frequency corresponding to a wavelength of $3l_0$ advected at $0.53U_0$, the present wave speed. Results for the two higher Reynolds numbers nearly collapse, but the peak at the lowest Reynolds number is lower, and has a larger low frequency content. Furthermore, figure 8(b) provides sample instantaneous one-dimensional deformation waves at three instants, t_1 , t_2 and t_3 , that are separated by a time gap of $50\nu/u_\tau^2$, all at $Re_\tau = 3300$. As is evident, the wave amplitude varies spatially and in time, making phase averaging extremely challenging. In contrast, Hristov & Plancarte (2014) and Hristov *et al.* (1998) show for field ocean waves that a Hilbert projection method can be used for estimating the

wave-coherent component of flow variables in the atmospheric boundary layer. Further details about this procedure, including a demonstration that it is effective in extracting the wave-coherent part of a flow variable, are provided in the [Appendix](#). The procedure involves the following steps. First, the wall deformation $d(x,z,t)$ is divided into multiple narrowband signals, $d_k(x,z,t)$, each with a frequency bandwidth of $\Delta\omega = 0.15U_0/l_0$. The division is performed in the Fourier domain, and each bandpass filtered signal is converted to the time domain. Second, the unsteady flow variable f' is projected onto each d_k using

$$\tilde{f} = \sum_k \left\{ \frac{\langle f', d_k \rangle}{\|d_k\|^2} d_k + \frac{\langle f', \mathcal{D}_k \rangle}{\|\mathcal{D}_k\|^2} \mathcal{D}_k \right\}, \quad (3.2)$$

where \mathcal{D}_k is the Hilbert transform of d_k , $\langle \cdot \rangle$ indicates an inner product and $\|\cdot\|^2$ is the squared norm. The [Appendix](#) shows that \tilde{d} has a 99.9 % correlation with d , i.e. they are nearly identical, and that the maximum $d-\tilde{p}$ and $d-\tilde{v}$ correlations exceed 96 % and 75 %, respectively. The remaining incoherent part of the signal, f'' , is obtained by subtracting the \tilde{f} from f' .

To verify that the wave coherent and stochastic turbulence are orthogonal, we have calculated the vertical profiles of the cross term, $\overline{\tilde{f}f''}$, and compared them with the corresponding coherent values for the streamwise and vertical velocity components as well as for the pressure. In all cases, the mean cross terms normalized by the corresponding coherent terms (not shown) remain below 10^{-7} , indicating that the wave-coherent motion and the stochastic turbulence are essentially orthogonal. It appears that the Hilbert projection method is effective even for the present non-stationary wave condition. Considering the small magnitudes of cross terms, they are neglected in subsequent discussions.

The next discussion compares the two-point correlation between the wall deformation and the wave-coherent flow variables with that between the deformation and the stochastic turbulence. The conditional correlation is conditioned on (i) a deformation magnitude exceeding d_{rms} , the local temporal r.m.s. deformation averaged over the entire area ([table 1](#)), and (ii) a surface peak (bump) or a minimum (dimple) at $\Delta x = 0$. The $\tilde{f}-d$ correlation for a bump is defined as

$$\begin{aligned} C_{\tilde{f}-d}(\Delta x, y, \Delta z) & \Big|_{d(x_0, z_0, t) > d_{rms}} \\ &= \frac{\langle \tilde{f}(x_0 + \Delta x, y, z_0 + \Delta z, t) d(x_0, z_0, t) \rangle \Big|_{d(x_0, z_0, t) > d_{rms}}}{\left(\langle \tilde{f}(x_0 + \Delta x, y, z_0 + \Delta z, t)^2 \rangle \langle d(x_0, z_0, t)^2 \rangle \right)^{\frac{1}{2}} \Big|_{d(x_0, z_0, t) > d_{rms}}}. \end{aligned} \quad (3.3)$$

A corresponding expression is used for a dimple. For the stochastic signal, \tilde{f} is replaced by f'' . The results for both a bump and a dimple are shown in [figure 9\(a,b\)](#). In each set, (i,iii,v,vii,ix) and (ii,iv,vi,viii,x) correspond to the $\tilde{f}-d$ and $f''-d$ correlations, respectively. Only results for $Re_\tau = 3300$ are presented here since those of the higher Reynolds numbers look very similar. The conditional wall shapes are plotted in (vii,viii), where the bump is bounded by dimples on both sides, and the dimple by bumps. The distance between dimples (or bumps), representing the characteristic wavelength of the deformation is $2.8l_0$, very close to the predicted theoretical value based on a linear analysis of the compliant wall response to harmonic excitations. The critical height is marked by a yellow dashed line. The conditional correlations of the coherent velocity and pressure based on bumps and dimples are essentially identical ([figure 9a](#)). Both are highly correlated with the deformation, with $C_{\tilde{u}-d}$ and $C_{\tilde{v}-d}$ having peaks of around ± 0.7 on both sides of the

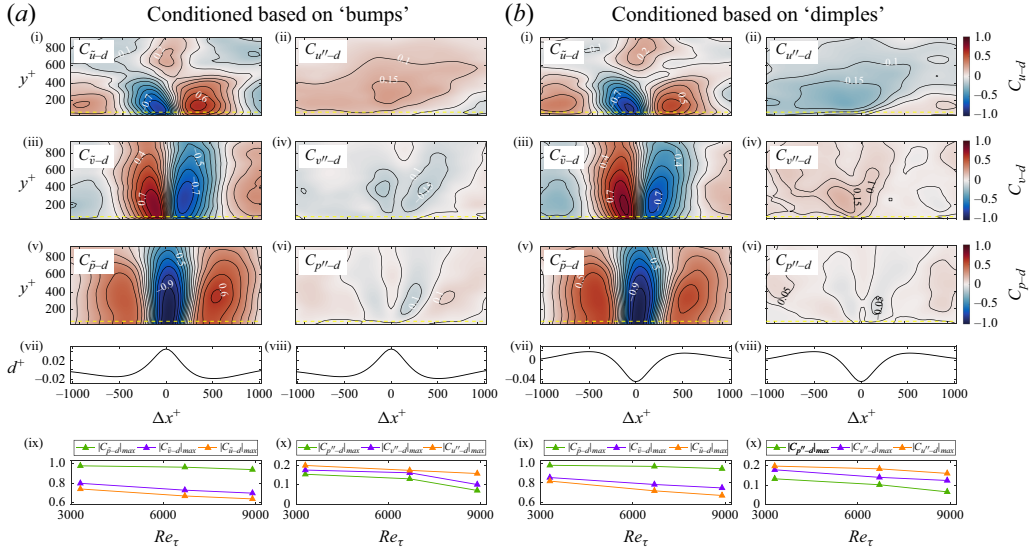


Figure 9. Conditional correlations of the deformation with the indicated flow variables based on (a) bumps, and (b) dimples, both at $Re_\tau = 3300$. In each set, subpanels (i), (iii), (v), (vii) and (ix) show the correlations with wave-coherent components ($C_{\tilde{f}-d}$), subpanels (ii), (iv), (vi), (viii) and (x) the correlation with the ‘stochastic’ turbulence ($C_{f''-d}$). The subpanels from (i) to (vi) show the distributions of C_{u-d} , C_{v-d} and C_{p-d} . Subpanels (vii) and (viii) present the conditionally averaged wall shape, and (ix) and (x), the variations of peak magnitudes of conditional correlations with Reynolds number.

bump/dimple. The domains of high correlation extend well above the critical layer, with the high $C_{\tilde{v}-d}$ peaks extending to further than those of $C_{\tilde{u}-d}$. Near the wall, the transitions between negative and positive $C_{\tilde{u}-d}$ are offset slightly downstream of the bump. Away from the wall, at $y^+ > 400$, the patterns switch phase for reasons discussed in the next section. In contrast, the transitions between negative and positive $C_{\tilde{v}-d}$ occur above the bump, and there are no phase shifts in the correlations at higher elevations. As expected, the $\tilde{p}-d$ correlations are negative above the bump, with values lower than -0.9 extending deep into the log layer and remaining below -0.5 at $y^+ = 900$. The minimum correlations, -0.98 , are measured at $y^+ = 90$, close to the critical height. The negative correlation peaks are bounded on both sides by positive peaks that also extend to $y^+ > 800$, with peak magnitudes of 0.6 aligned with the deformation troughs in the data conditioned on bumps, and bumps in the analysis conditioned on dimples. The implications and flow phenomena associated with these patterns are discussed in the next section. In contrast, the incoherent velocities and pressures are poorly correlated with the deformation, confirming that the f'' variables are incoherent with the deformation. The correlations with the incoherent velocity components (u'' and v''), conditioned on bumps and dimples, have opposite signs with peak magnitudes remaining below 0.2 . They indicate a broad sweeping flow above the bump, and a diminishing sweeping flow above the dimple, with $C_{v''-d} > 0$ to the left of the dimple and nearly zero to the right of it. There is also non-zero but very low correlation with the pressure, indicating a weak minimum above the bump, and a weak maximum above the dimple. It should be noted, as discussion follows, that except for the pressure near the wall, for most of the flow field, the magnitudes of u'' , v'' and p'' are substantially higher than the corresponding coherent variables. Furthermore, as shown in subpanels (ix) and (x), the peak correlation magnitudes involving coherent variables, namely the highest values of $C_{\tilde{u}-d}$, $C_{\tilde{v}-d}$ and $C_{\tilde{p}-d}$, decrease with increasing Reynolds number. This decrease occurs in spite of the increase in the scaled deformation

height (table 1). Finally, the maxima of $C_{u''-d}$, $C_{v''-d}$ and $C_{p''-d}$ magnitudes, which are also presented in subpanels (ix) and (x), remain low and decrease with increasing Reynolds number.

In addition, while the magnitudes of the $u''-d$ correlations for a bump and a dimple are low, their inclination and elongation resemble those of $u'-u'$ correlations in a typical rigid wall boundary layer (e.g. Ganapathisubramani *et al.* 2005; Sillero, Jiménez & Moser 2014). This trend likely arises from the fact that conditional correlations are restricted to deformations exceeding the r.m.s. value. Such a restriction might cause a weak bias towards sweeping motions, where the near wall velocity is elevated, and the flow is subjected to adverse pressure gradients. Furthermore, the inclination angle of the $u''-d$ correlation is $\sim 15^\circ$, consistent with that of the $u'-u'$ correlation in a solid wall boundary layer, a trend that has been associated with coherent structures (Ganapathisubramani *et al.* 2005; Adrian 2007; Jiménez 2018). This trend suggests that high wall deformations might be weakly correlated with ‘naturally occurring’ coherent structures in the boundary layer.

Figure 10 presents the distributions of phase-averaged coherent flow field, \hat{f} , as a function of deformation phase, at the three Reynolds numbers. The phase averaging is performed by dividing a wave cycle into 20 phase bins, i.e. each with a width of $\pi/10$, and averaging all the data ($> 8.8 \times 10^5$ samples) inside each bin. The wall-normal axis is scaled both as y/y_c and y/δ , with the results for $Re_\tau = 3300$, 6700 and 8900 plotted in figures 10(a,b), 10(c,d) and 10(e,f), respectively. The phase-averaged wall deformation is presented in figure 10(g) and repeated three times for convenience. Note that the phase-averaged dimples are slightly deeper than the bumps, consistent with the PDFs of deformation in figure 3, e.g. at $Re_\tau = 8900$, $d_{max} \approx -0.93d_{min}$. For all the three cases, when the vertical axis is scaled with outer variables, they display similar distributions of flow quantities penetrating deep into the log layer in spite of substantial differences in the heights of the deformation. The velocity contours have alternate signs, which are not in phase with the windward ($-\pi < \phi < 0$) or leeward ($0 < \phi < \pi$) sides. The \hat{u} contours (figure 10a,c,e) are inclined upstream at $y/\delta \leq 0.15$, and shift significantly at $y/\delta \sim 0.19$. Near the wall, the velocity vectors indicate Q2 events (ejections, $\hat{u} < 0$, $\hat{v} > 0$) generally on the windward side and near the crest, and Q4 events (sweeps, $\hat{u} > 0$, $\hat{v} < 0$) on the leeward side and the trough. The distribution of \hat{v} appear to be periodic at all elevation, with positive values above the windward side and negative on the leeward side, without the phase shift observed in the horizontal velocity.

Due to the Q2 and Q4 events, the horizontal velocity maxima are located slightly above the critical layer, whereas the coherent vertical velocity maxima extend to around three times the critical height. Overall, the coherent velocity peaks decrease with increasing Reynolds numbers, in contrast with the increase in deformation height. Further understanding of the flow structure can be obtained by examining the corresponding distributions of $\hat{\omega}_z$ and \hat{p} presented in figure 11. Like the velocity, the vorticity and pressure magnitudes decrease with increasing Reynolds number. Below the critical height, $\hat{\omega}_z$ (figure 11a,c,e) is negative on the leeward side and positive on the windward side. This pattern shifts at higher elevations, where the $\hat{\omega}_z < 0$ region is aligned with the top of a bump, and $\hat{\omega}_z > 0$ with the trough. At $y > y_c$, the transitions between positive and negative areas remain largely vertical. The negative regions in the distributions of pressure (figure 11b,d,f) appear to be aligned with the wave crests, with the peaks around $\pi/10$ ahead of the summits. The positive peaks are aligned with the troughs, with their maxima also located approximately $\pi/10$ ahead of the valleys. The $\sim \pi/10$ phase shift is consistent with the trends of $p'-d$ correlations reported in Zhang *et al.* (2017) for an order of magnitude stiffer compliant wall, as inferred from the offset of the peak correlation and

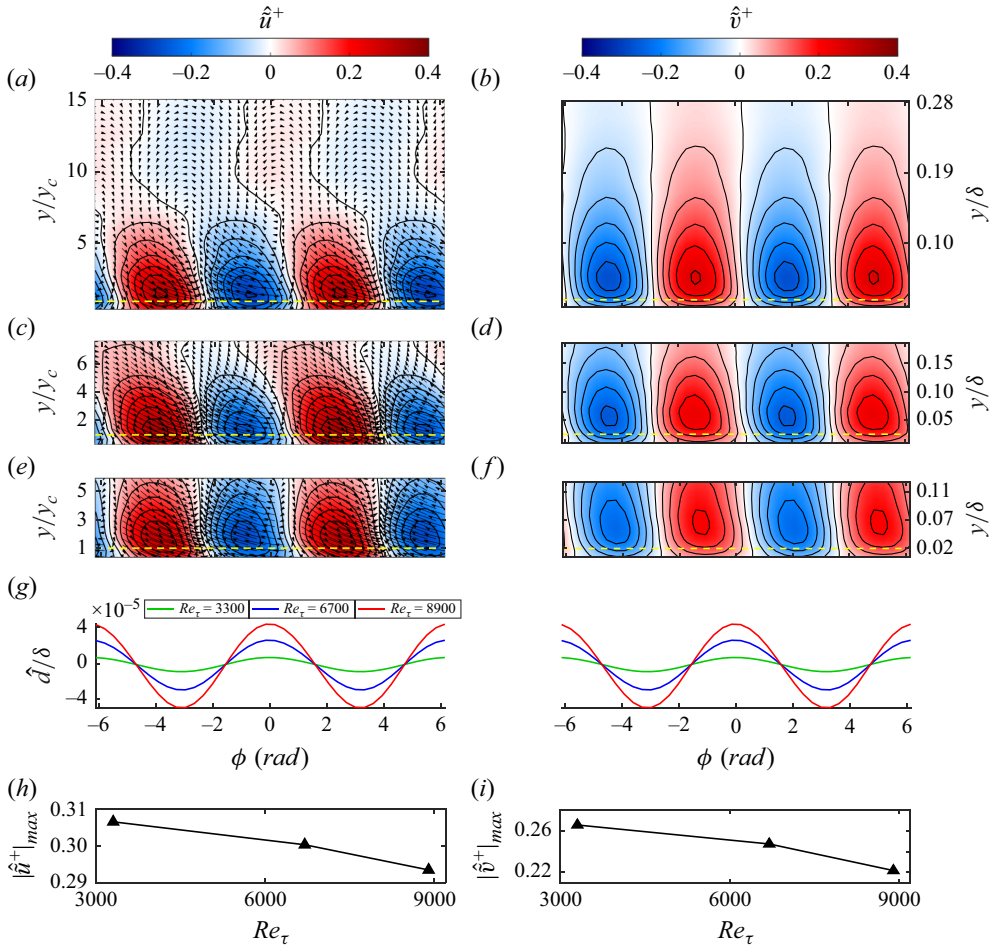


Figure 10. Variations of the wave-coherent, spatially and temporally phase-averaged: (a,c,e) \hat{u}^+ , (b,d,f) \hat{v}^+ and (g) \hat{d}/δ with deformation phase; (a,b) $Re_\tau = 3300$, (c,d) $Re_\tau = 6700$ and (e,f) $Re_\tau = 8900$. The arrows in (a,c,e) show the velocity vectors, and the yellow dashed lines indicate the critical heights. Panels (h) and (i) display the variations of peak (h) \hat{u}^+ and (i) \hat{v}^+ with Reynolds number.

the deformation wavelength. They attribute this delay primarily to the flow structure in the boundary layer, and to a lesser extent, to the material response. Esteghamatian *et al.* (2022) also observe a similar phase lag, but in their case, the delay decreases with the deformation magnitude, e.g. from $\sim \pi/4$ at $d_{rms}^+ = 5.6$ to $\sim \pi/8$ at $d_{rms}^+ = 0.55$. Finally, figures 10(h,i) and 11(h,i) show that for all the flow variables presented in figures 10 and 11, the magnitudes of the coherent parts decrease with increasing Reynolds number in spite of the significant increase in d_{rms}^+ . A plausible cause for these contradicting trends is discussed later in the paper.

The locations of the negative and positive vorticity peaks above the crest and trough, respectively, are consistent with results of conditional averaging of the flow structures above bumps and dimples, without decomposition to coherent and stochastic turbulence, as mentioned briefly (but not shown) in Lu *et al.* (2024). Here, the conditional averaging also uses $d > d_{rms}$ for a surface bump and $d < d_{rms}$ for a dimple. The results of this conditional sampling, which is summarized in figure 12, show that bumps preferentially form under

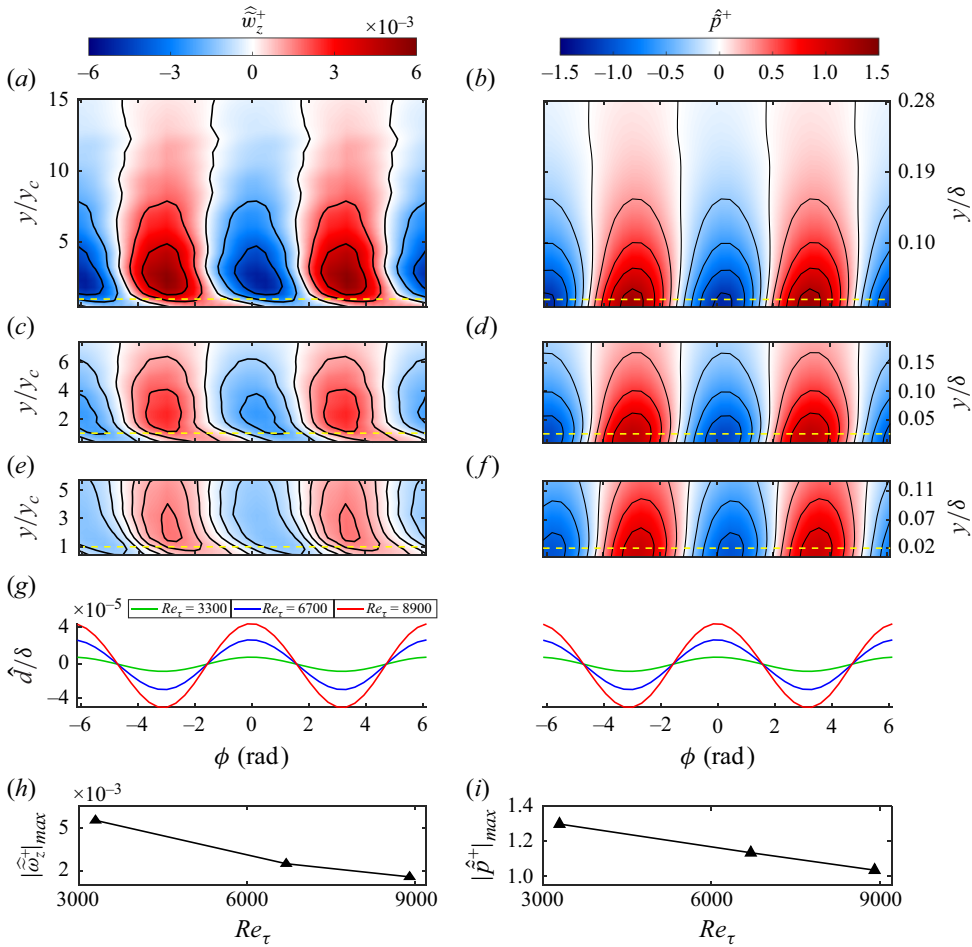


Figure 11. Variations of the wave-coherent, spatially and temporally phase-averaged: (a,c,e) \hat{w}_z^+ , (b,d,f) \hat{p}^+ , and (g) \hat{d}/δ with deformation phase; (a,b) $Re_\tau = 3300$, (c,d) $Re_\tau = 6700$ and (e,f) $Re_\tau = 8900$. The yellow dashed lines indicate the critical heights. Panels (h) and (i) display the variations of peak (h) \hat{w}_z^+ and (i) \hat{p}^+ with Reynolds number.

a negative spanwise vortex, owing to the pressure minimum that this vortex generates (figure 12a,c). A sweeping flow induced downstream of this vortex impinges on the surface, generating a pressure maximum and a dimple at the sweep to ejection transition (figure 12b,d). The present coherent part of the flow contains a negative vorticity peak above the bump, where the pressure is minimum, and a sweeping-ejection transition above the dimple, where the pressure is maximum. In attempts to explain the curious shift in the vorticity distribution below the critical height, one possibility is generation of counter rotating vorticity as the vortical structure above interacts with the boundary, generating shear in the opposite direction. Another possibility might involve viscous vorticity flux from the wall associated either with the pressure gradients (Lighthill 1963) or the surface-parallel material acceleration (Morton 1984). These two contributors are compared based on DNS data by Esteghamatian *et al.* (2022). Results show these two contributors have opposite effects, with a net impact that varies with the compliant material stiffness and amplitude of the deformation. Unfortunately, the present data does not have sufficient

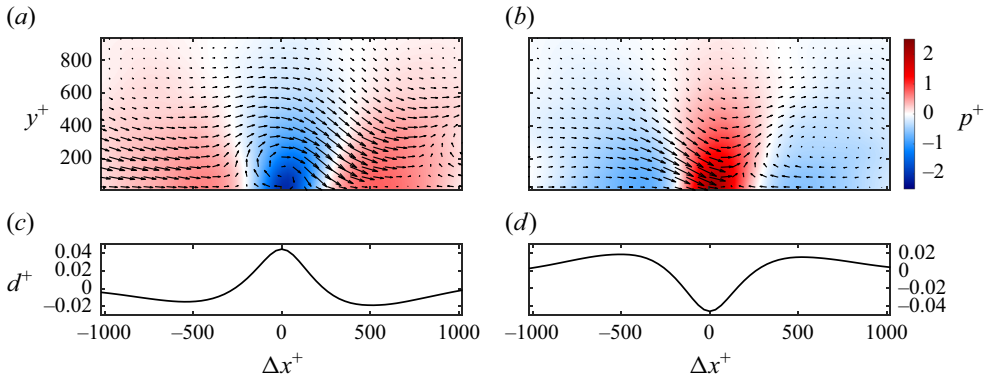


Figure 12. Conditionally averaged flow variables and deformation at $\Delta z^+ = 0$ for (a,c) a surface bump, and (b,d) a dimple, both at $Re_\tau = 3300$: (a,b) pressure contours and in-plane velocity vectors, and (c,d) compliant wall shape.

spatial resolution to determine the near wall vorticity or the surface acceleration, so we cannot comment on the viscous vorticity diffusion. Esteghamatian *et al.* (2022) also show for relatively large deformation ($d_{rms}^+ = 5.6$), thickening of the boundary layer and flow separation close to the wave crest inject negative vorticity to the flow above the trough. However, the present deformations are significantly smaller, and the vorticity distribution shift occurs also for $d_{rms}^+ \ll 1$ (figure 11a,c,e). Hence flow separation is unlikely to be a significant contributor. This discussion suggests that the first option, namely formation of counter-rotating vorticity as the flow induced by a vortex interacts with the wall, seems to be the most viable option.

Before proceeding, it should be noted that the present distributions of \hat{u} and \hat{v} are not consistent with results obtained for wind-wave interactions (e.g. Buckley & Veron 2019; Cao & Shen 2021; Do, Wang & Chang 2024), and the simulated flow over a very soft compliant material (Esteghamatian *et al.* 2022). Discrepancies exist also among results obtained for ocean waves owing to differences in wave amplitude, slope and ‘age’ (U_{sw}/u_τ). There is better consistency among the distributions of pressure, where the minima are persistently centred in the vicinity of the wave crest, and the maxima around the trough. The differences from Esteghamatian *et al.* (2022) might be related to the more than an order of magnitude higher wave amplitude owing to the much softer material in their simulations. Consequently, their wave crest is more prone to flow separation. Another possibility is related to the relationship between wave speed and flow velocity, which might affect the compliant wall–flow interactions. In the simulations, the magnitude of U_{sw} is close to the shear wave speed, corresponding to the advection speed of Rayleigh waves in elastic material ($\sim 0.95C_t$, Freund 1998). In contrast, in the present experiments as well as the data presented in Carpenter *et al.* (2000), Zhang *et al.* (2017), Wang *et al.* (2020), Greidanus *et al.* (2022) and Lu *et al.* (2024), U_{sw} varies between 40 %–80 % of U_0 and does not scale with C_t .

Questions remain whether it is possible to relate the unsteady wave-coherent motion to the flow induced by a steady wall roughness. Nakato *et al.* (1985) suggest that a rough wall boundary layer should be considered as flow over a wavy surface when the roughness slope is less than 6° . In this case, the momentum deficit in the log layer is strongly affected by the slope of the roughness element, increasing from ~ 1 to ~ 9.5 when the slope increases from 1° to 6° (e.g. Napoli, Armenio & Marchis 2008; Schultz & Flack 2009). In the present study, the slope changes, 0.01° to 0.07° , are two orders of magnitude smaller, yet the

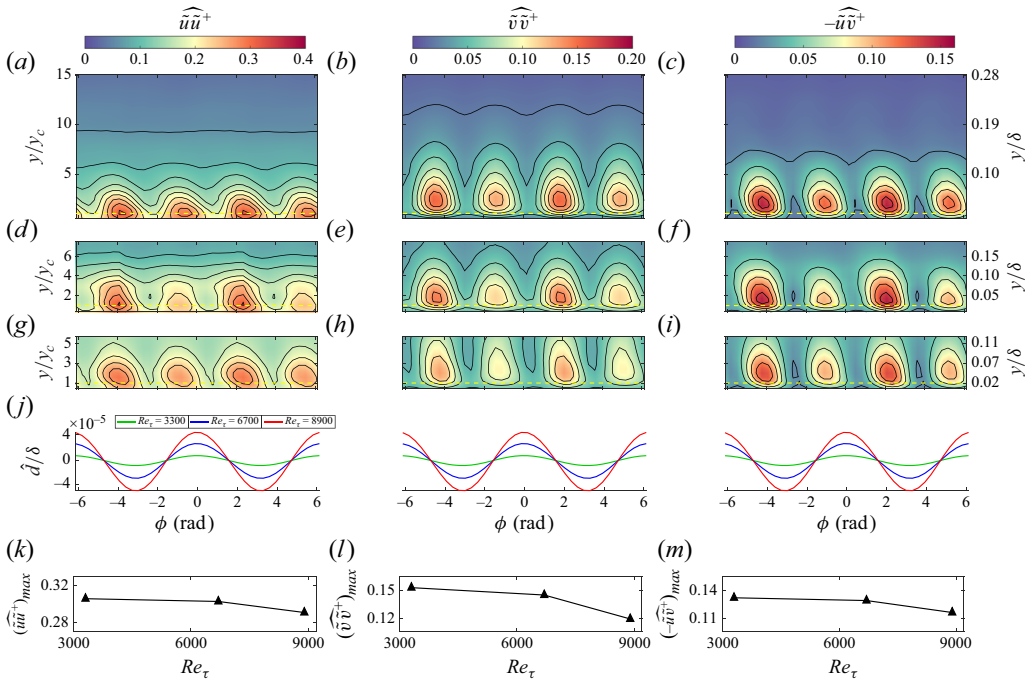


Figure 13. Variations of the wave-coherent, spatially and temporally phase-averaged: (a,d,g) $\widehat{u'u'}$, (b,e,h) $\widehat{v'v'}$, (c,f,i) $-\widehat{u'v'}$ and (j) $\widehat{d/\delta}$ with deformation phase: (a–c) $Re_\tau = 3300$, (d–f) $Re_\tau = 6700$ and (g–i) $Re_\tau = 8900$. Yellow dashed lines indicate the critical heights. Panels (k–m) display the variations of peak (k) $\widehat{u'u'}$, (l) $\widehat{v'v'}$ and (m) $-\widehat{u'v'}$ with the Reynolds number.

downward shifts in velocity profiles increase from 1.1 to 2.6, i.e. it is of the same order as that of the rough wall. However, in the present measurements, the deformation amplitude also increases with the Reynolds number, which is also expected to affect the momentum deficit. Furthermore, the flow over stationary wavy surfaces with low slopes has also been modelled theoretically by Hunt, Leibovich & Richards (1988). This model assumes that the wave amplitude and the roughness length are much smaller than wavelength, conditions that are satisfied in the present experiments. They divide the flow field into an inner region, where surface-induced shear stress is significant, and an outer region, where the flow perturbations are inviscid. The present measurements do not resolve the inner region. In the outer region, the present coherent vertical velocity component (figure 10b,d,f) peaks at the elevation as the theoretical prediction. However, the present coherent horizontal velocity peaks in the outer layer, in contrast to the model prediction that places this peak in the inner layer. Therefore, some of the trends of the compliant wall boundary layer appear to be consistent with those of the flow over a stationary surface undulation, while others do not.

The next discussion compares the magnitudes of $\widetilde{u_i u_j}$ with those of $u_i'' u_j''$, and $\widetilde{p_{rms}}$ with p_{rms}'' . As figure 13 demonstrates, all the coherent stresses are concentrated near the wall, decaying rapidly with elevation. The values of $\widehat{u'u'}$ peak at or just above the critical layer, and those of the other stresses, at higher elevations, all consistent with the peak locations of their mean values. All the coherent stresses have maxima on the windward and leeward sides, which are asymmetric both in phase and in magnitude. The phase lags are consistent with the delay between the coherent velocity and the deformation, as depicted

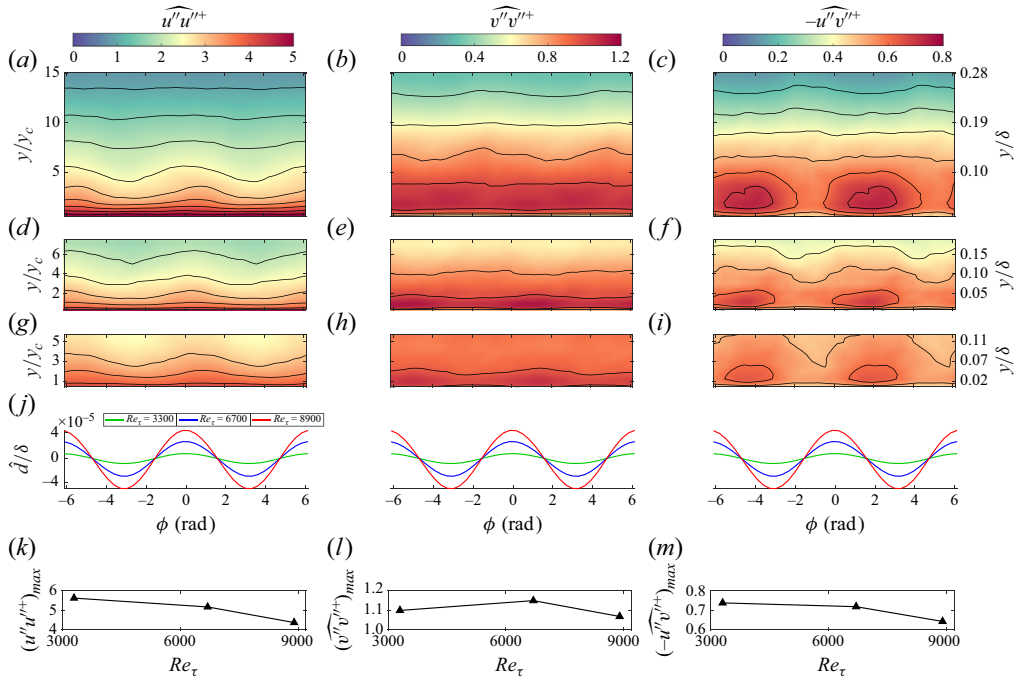


Figure 14. Variations of the stochastic, spatially and temporally phase-averaged: (a,d,g) $\widehat{u''u''^+}$, (b,e,h) $\widehat{v''v''^+}$, (c,f,i) $-\widehat{u''v''^+}$ and (j) \widehat{d}/δ with deformation phase; (a–c) $Re_\tau = 3300$, (d–f) $Re_\tau = 6700$ and (g–i) $Re_\tau = 8900$. Panels (k–m) display the variations of peak (k) $\widehat{u''u''^+}$, (l) $\widehat{v''v''^+}$ and (m) $-\widehat{u''v''^+}$ with the Reynolds number.

in figure 10. All the stresses are stronger on the leeward side, and decrease with increasing Reynolds number, trends that are evident in figure 13(k–m). The difference between the windward and leeward values appears to be associated with infrequent, high amplitude sweep–ejection events above the troughs. The formation of stress maxima on the windward and leeward sides is consistent with the DNS data in Esteghamatian *et al.* (2022), with some phase differences. The simulations also show strong negative shear stress peaks between the positive maxima very near the wall ($y^+ \leq 4$), which the experimental data cannot resolve.

Figure 14 presents the phase-averaged distributions of $u''_i u''_j$ for the three Reynolds numbers. As is evident, the magnitudes of the incoherent stresses are higher than the coherent ones by nearly an order of magnitude everywhere, indicating that most of the unsteady motion is incoherent, and that the trends with elevation are consistent with those of the total Reynolds stresses. In particular the maximum in $-\widehat{u''v''}$ at the two higher Reynolds number occurs at the critical height. While the variations of $u''u''$ and $-\widehat{u''v''}$ with deformation phase are milder than those of the coherent motions, the ‘stochastic’ stresses are still not distributed uniformly. Both $\widehat{u''u''}$ and $-\widehat{u''v''}$ peak on the downwind sides of the bump, with the maxima in $\widehat{u''u''}$ occurring upstream of those of $-\widehat{u''v''}$. Their variations with phase seem to decrease with increasing Reynolds number. Since the leeward side experience an adverse pressure gradient, the turbulence level is expected to increase. Interestingly, the peaks in $\widehat{u''u''}$ do not occur in the same phase as those of $\widehat{u''v''}$, but the maxima in $-\widehat{u''v''}$ and $-\widehat{u''v''}$ do coincide. The distributions of $\widehat{v''v''}$ are more uniform, and do not display consistent or clear trends with Reynolds number. As discussed later, these

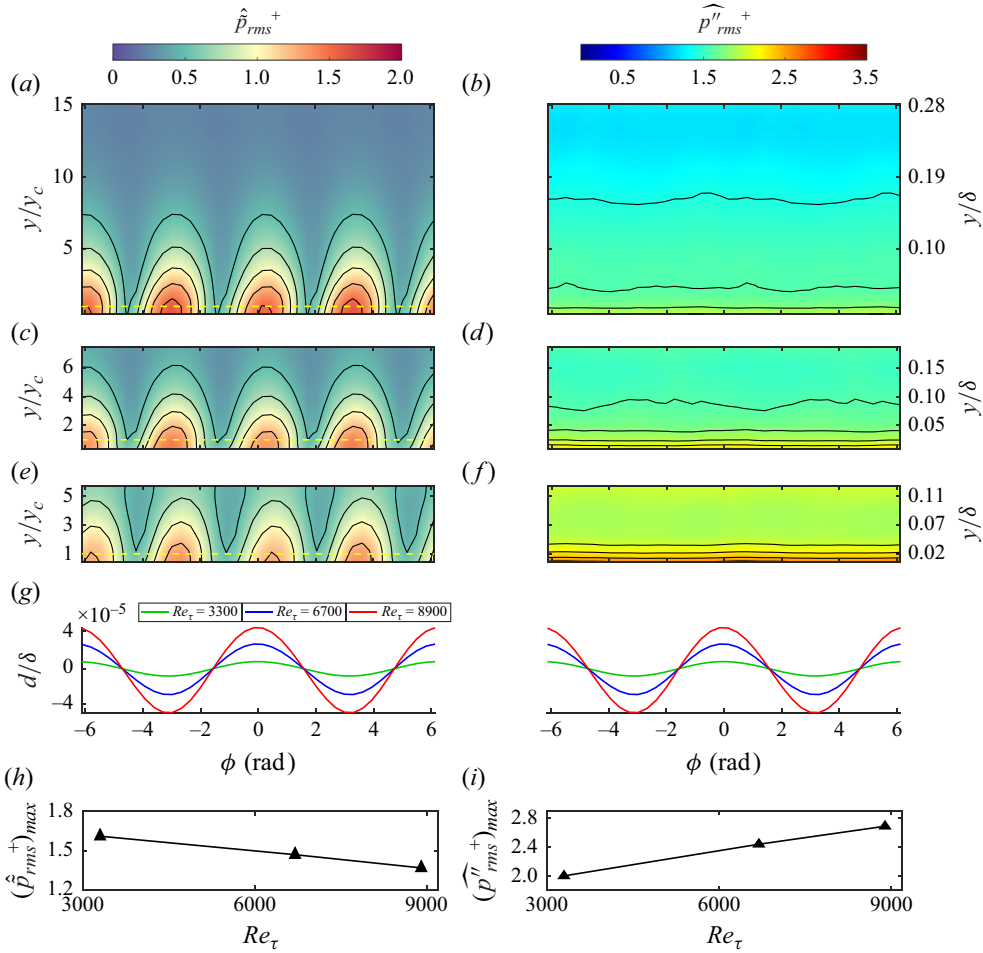


Figure 15. Variations of the spatially and temporally phase-averaged: (a,c,e) \hat{p}_{rms}^+ , (b,d,f) \hat{p}''_{rms}^+ and (g) \hat{d}/δ with deformation phase: (a,b) $Re_\tau = 3300$, (c,d) $Re_\tau = 6700$ and (e,f) $Re_\tau = 8900$. Panels (h,i) display the variations of peak (h) \hat{p}_{rms}^+ , and (i) \hat{p}''_{rms}^+ with Reynolds number.

phase variations will affect the energy exchange between the coherent and incoherent parts of the kinetic energy.

The phase-averaged distributions of coherent and stochastic r.m.s. pressure are compared in figure 15. The coherent r.m.s. pressure peaks are concentrated near the wall, peaking slightly beyond the crest and the trough of the deformation (figure 15a,c,e), and their magnitudes decrease with increasing Reynolds number (figure 15h). The stochastic r.m.s. pressure also peaks at the wall but does not vary significantly with phase (figure 15b,d,f). In contrast to the coherent values, the stochastic r.m.s. pressure increases with Reynolds number (figure 15i). Owing to these opposite trends, while the coherent and stochastic maxima have similar magnitudes at $Re_\tau = 3300$, the stochastic r.m.s. is more than twice higher than that at $Re_\tau = 8900$.

3.3. Kinetic energy budgets for wave-coherent flow and stochastic turbulence

Following the established framework, the total turbulent kinetic energy can also be separated into a coherent ‘wave kinetic energy’ (WKE), and an incoherent ‘stochastic

kinetic energy' (SKE),

$$\frac{1}{2}\overline{u'_i u'_i} = \frac{1}{2}\overline{\tilde{u}_i \tilde{u}_i} + \frac{1}{2}\overline{u''_i u''_i}. \quad (3.4)$$

As verified before, the cross terms are negligible since \tilde{u}_i and u''_i are uncorrelated. Following Reynolds & Hussain (1972), the turbulent kinetic energy budget equation is also decomposed. The WKE budget is given by

$$\begin{aligned} 0 = & (-\overline{\tilde{u}_i \tilde{u}_j}) \partial_j \bar{u}_i + \overline{(\tilde{u}'_i \tilde{u}'_j)} \partial_j \tilde{u}_i - \partial_j (\overline{\tilde{u}_j \tilde{p}}) - \bar{u}_j \partial_j (0.5 \overline{\tilde{u}_i \tilde{u}_i}) - \partial_j [\overline{\tilde{u}_j (0.5 \tilde{u}_i \tilde{u}_i)}] \\ & - \partial_j \left[\overline{\tilde{u}_i (\tilde{u}'_i \tilde{u}'_j)} \right] + \nu \partial_j [\overline{\tilde{u}_i (\partial_j \tilde{u}_i + \partial_i \tilde{u}_j)}] - 2\nu \overline{(\partial_j \tilde{u}_i + \partial_i \tilde{u}_j) (\partial_j \tilde{u}_i + \partial_i \tilde{u}_j)}, \end{aligned} \quad (3.5)$$

where $(-\overline{\tilde{u}_i \tilde{u}_j}) \partial_j \bar{u}_i$ is the WKE production by mean flow; $\overline{(\tilde{u}'_i \tilde{u}'_j)} \partial_j \tilde{u}_i$ is the WKE production by the stochastic turbulence; $-\partial_j (\overline{\tilde{u}_j \tilde{p}})$ is the coherent pressure diffusion; $-\bar{u}_j \partial_j (0.5 \overline{\tilde{u}_i \tilde{u}_i})$ is the advection by mean flow; and the fifth to seventh terms represent the transport of WKE by the wave-coherent stresses, stochastic turbulent stresses and viscous stresses, respectively. The last term is the viscous dissipation. Accordingly, the budget equation for the SKE is

$$\begin{aligned} 0 = & (-\overline{u'_i u'_j}) \partial_j \bar{u}_i - \overline{(u''_i u''_j)} \partial_j \tilde{u}_i - \partial_j (\overline{u'_j p''}) - \bar{u}_j \partial_j (0.5 \overline{u'_i u'_i}) - \partial_j [\overline{u'_j (0.5 u'_i u'_i)}] \\ & - \tilde{u}_j \partial_j (0.5 \overline{u'_i u'_i}) + \nu \partial_j \left[\overline{u'_i (\partial_j u'_i + \partial_i u'_j)} \right] - 2\nu \overline{(\partial_j u'_i + \partial_i u'_j) (\partial_j u'_i + \partial_i u'_j)}, \end{aligned} \quad (3.6)$$

where $(-\overline{u'_i u'_j}) \partial_j \bar{u}_i$ and $-\overline{(u''_i u''_j)} \partial_j \tilde{u}_i$ are production of SKE by the mean flow and the wave-coherent motions, respectively. The other terms follow the same order as those associated with WKE. One term, $\overline{(u'_i u''_j)} \partial_j \tilde{u}_i$, appears in both equations with the opposite sign, representing transfer of energy from the stochastic turbulence to the wave-coherent motions when positive.

The profiles of WKE and SKE budget terms at $Re_\tau = 3300$ are compared in figure 16. As is evident, near the wall, the production by mean flow is larger than the rest of the terms by more than an order of magnitude, with shear productions, namely $(-\tilde{u}\tilde{v})\partial\bar{u}/\partial y$ and $(-u''v'')\partial\bar{u}/\partial y$, being the dominant contributors. Near the wall, the WKE production is only 6%–10% of the SKE counterpart, decreasing to 3% in the log layer. Figure 17(a,b) shows the variations of shear production terms with Reynolds number. When plotted using inner variables, the profiles of both production terms collapse far away from the interface, but they deviate near the wall, consistent with the reduction of the stochastic and coherent shear stresses with increasing Reynolds number. Trends do not collapse when plotted using mixed variables either (insert in figure 17a). While the stresses nearly collapse, the mean velocity gradients do not. Both production terms still increase with decreasing elevation at the lowest point that can be resolved by the present 3-D measurements, implying that both terms peak below the critical height. For the resolved range, the profiles of SKE production (figure 17b) are consistent with those obtained in DNS of a smooth rigid wall channel flow at $Re_\tau = 5200$ (Lee & Moser 2015), especially in the outer layer. However, compliant wall boundary layer DNS (Esteghamatian *et al.* 2022) shows that the Reynolds stress becomes negative at $y^+ < 4$, implying that reverse energy transfer, from the wave to the mean flow, occurs very near the wall. Finally, figures 17(c) and 17(d) compare the variation of shear production terms with wave phase. In accordance with the distributions of shear stresses,

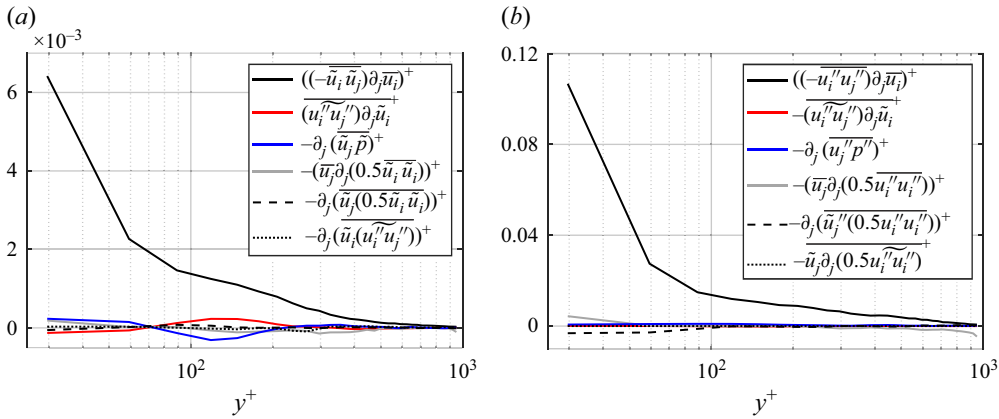


Figure 16. Wall-normal profiles of the ensemble-averaged kinetic energy budget terms for: (a) WKE and (b) SKE, both at $Re_\tau = 3300$.

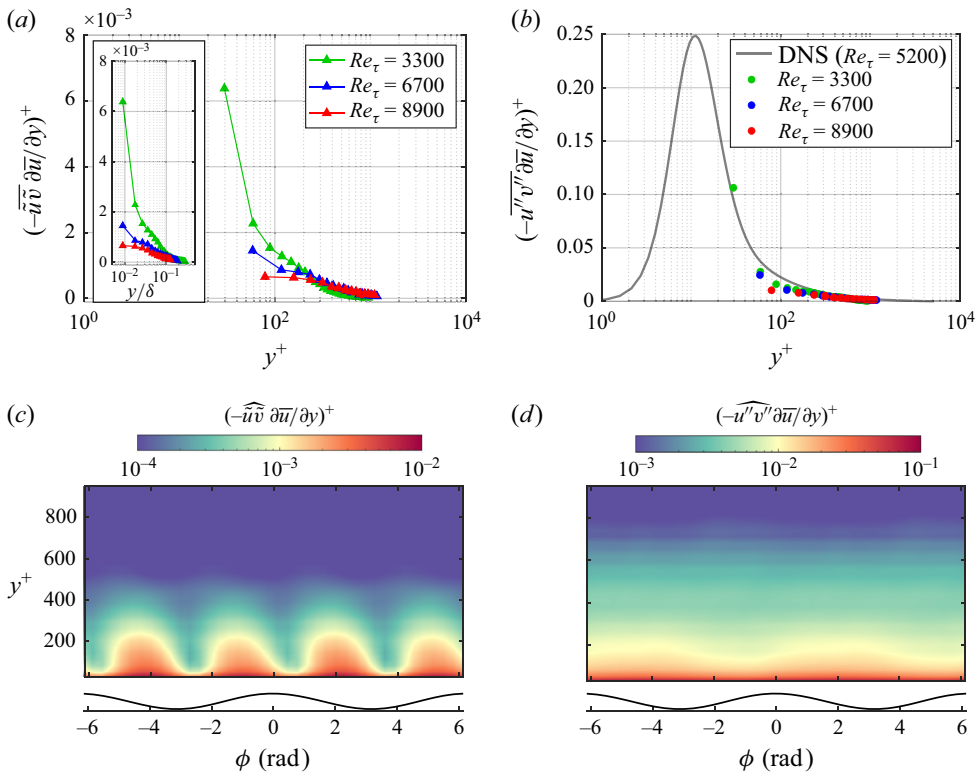


Figure 17. Shear production rates: (a,b) ensemble-averaged profiles of (a) WKE, and (b) SKE at the indicated Reynolds numbers; (c,d) distributions of (c) $(-\widehat{u\tilde{v}} \partial \tilde{u} / \partial y)^+$ and (d) $(-\widehat{u''v''} \partial \tilde{u} / \partial y)^+$ at $Re_\tau = 3300$.

the WKE production peaks are located slightly upstream of the crest and the trough. The variation in SKE production with phase is milder, with higher values on the leeward side, in the same area as the phase-averaged transition from sweep to ejection.

The next discussion shifts to the energy exchange between WKE and SKEs. Consistent with trends of wind-wave interaction (Zhang, Wang & Liu 2024), the axial

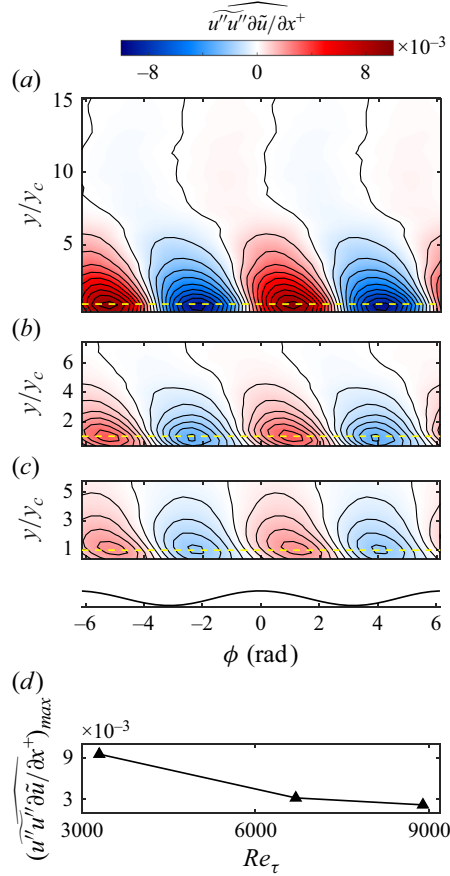


Figure 18. The axial contributor to wave–turbulence energy exchange: (a,b,c) temporally and spatially phase-averaged distributions at (a) $Re_\tau = 3300$, (b) $Re_\tau = 6700$ and (c) $Re_\tau = 8900$. (d) Variations of the peak values with Reynolds number.

extension/contraction term, i.e. $\overline{(u''u'')}\partial\tilde{u}/\partial x$, is the dominant contributor. Plots of the phase-averaged axial contraction (figure 18a–c) indicate that this term is negative on the windward side, i.e. energy is transferred from WKE to SKE owing to the wave-induced streamwise contraction, and positive on the leeward side, owing to axial extension. The net energy flux is therefore the difference between the contributions of contraction and extension. At all three Reynolds numbers, the axial contraction and extension peaks are aligned along the critical height but decrease in magnitude with increasing Re_τ (figure 18d). Profiles of the net energy fluxes (figure 19) are presented scaled using inner variables (figure 19a), and mixed variables, u_τ^3/λ (figure 19b), where the wall unit is replaced by the surface wavelength ($\lambda = 3l_0$). Both have been used for normalizing data in studies of wind–wave interaction (e.g. Yousefi *et al.* 2021; Zhang *et al.* 2024). With either scaling, the magnitudes of energy flux decrease with increasing Reynolds number, but the differences between them are significantly smaller under mixed scaling. Finally, the energy fluxes at all the three Reynolds numbers change sign across the critical layer. At $y > y_c$, kinetic energy is transferred from the stochastic turbulence to the wave-coherent field. Conversely, at $y < y_c$, kinetic energy flows from the coherent to the stochastic turbulence. A sign change across the critical layer is also observed in the coherent pressure diffusion,

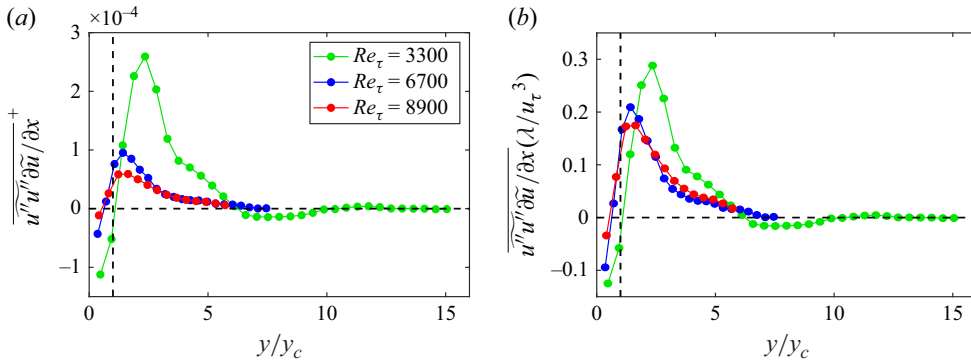


Figure 19. Wall-normal profiles of the ensemble-averaged axial wave–turbulence energy exchange term for the three Reynolds numbers, normalized using (a) inner and (b) mixed parameters.

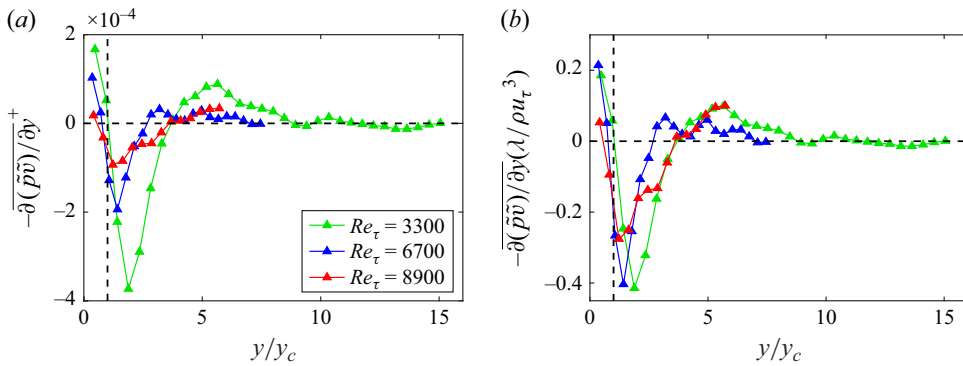


Figure 20. Wall-normal profiles of the ensemble-averaged coherent pressure diffusion term for the three Reynolds numbers, normalized using (a) inner and (b) mixed parameters.

in which the wall-normal gradient of the \tilde{p} – \tilde{v} correlation is the main contributor. Profiles of the ensemble averaged values (figure 20a,b) indicate that mixed scaling leads to better collapse of results than the inner variables. In contrast to the wave–turbulence exchange, pressure diffusion adds energy to the wave-coherent field at $y < y_c$ and depletes it at $y > y_c$. A comparison with the profiles of WKE, shown in figure 21, indicates that the peak negative pressure diffusion is located at nearly the same elevation as the maximum WKE, and the sign change indicates transport towards the wall, across the critical layer.

4. Discussion

In the previous sections we have noticed that in contrast to the substantial increase in surface wave amplitude with increasing Reynolds number, the coherent phase-averaged velocity, vorticity and pressure, as well as the coherent stresses, r.m.s. pressure, kinetic energy, WKE production rate and WKE–SKE exchange decrease. Furthermore, both the p' – d correlation and coherence, presented in Lu *et al.* (2024) and reproduced as figure 22 decay with increasing Reynolds number at all elevations. This section attempts to discuss possible reasons for these apparently contradicting trends, namely that all the parameters associated with flow–deformation interaction are strongest while the deformation height is the smallest at the lowest Reynolds number. Furthermore, figure 22(a) also shows the p' – d correlation of the one-way coupling case in Zhang *et al.* (2017), which as noted before,

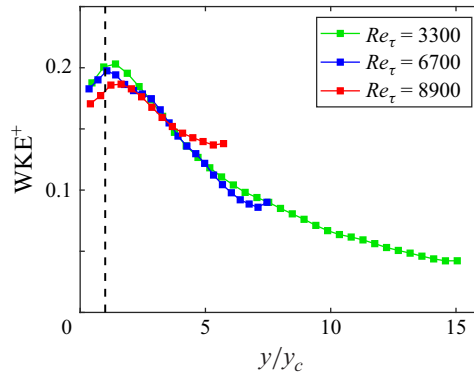


Figure 21. Wall-normal profiles of the WKE at the indicated Reynolds numbers.

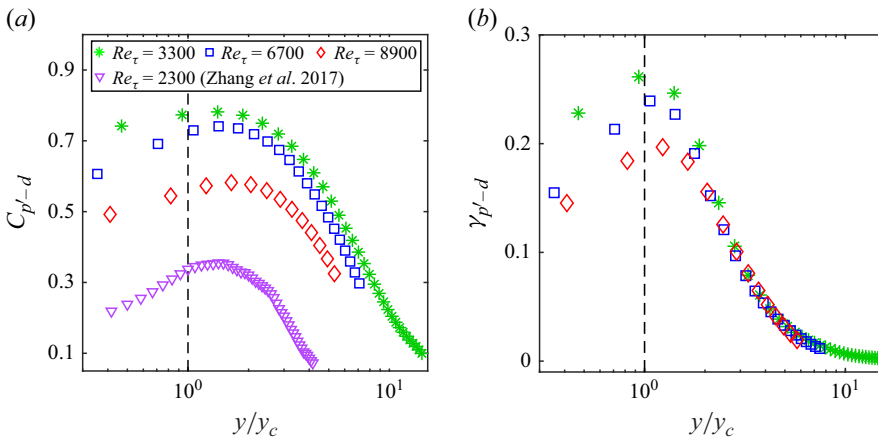


Figure 22. Wall-normal profiles of the (a) p' - d correlation conditioned on a bump for the present and the Zhang *et al.* (2017) data, and (b) p' - d coherence for the present data, both at the indicated Reynolds numbers. The present results are reproduced from Lu *et al.* (2024).

involves a thicker and stiffer compliant material ($l_0 = 16$ mm, $E = 930$ Kpa). Clearly, the latter is considerably lower than those of the present experiments, despite the agreement in the magnitude of d_{rms}^+ (~ 0.03), and the similarity in Re_τ to the present slowest case. The analysis aimed at explaining these disagreements is based on a comparison between the wavelength of energy containing eddies in the boundary layer and the characteristic wavelength of the deformation.

In the compliant wall turbulent boundary layer, the interaction between flow and deformation is not restricted to a single wavelength. Some of the theoretical approaches examine the deformation as surface responses to harmonic flow excitations at different frequencies and wavenumbers (e.g. Chase 1991; Benschop *et al.* 2019). Therefore, it is necessary to compare the length scales of the turbulent structures in the boundary layer with the wavelength and frequency dependent responses of the compliant surface deformation. The former has been studied extensively in smooth-wall boundary layers, both experimentally (e.g. Mathis, Hutchins & Marusic 2009) and numerically (e.g. Jimenez *et al.* 2010). The boundary layer scales, denoted as λ_x in the following discussion, vary from the viscous length scales to several times the boundary layer thickness. The energetic coherent structures, characterized by the spectral domain with a slope of -1

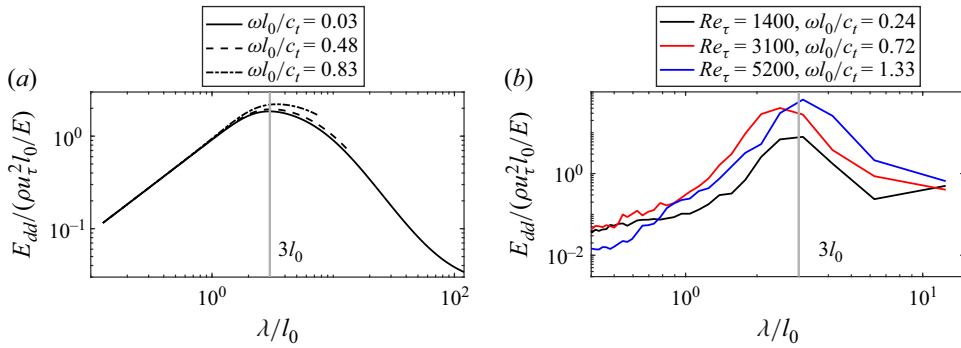


Figure 23. Wavelength of the compliant surface response at the indicated frequencies, based on (a) a solution to the Chase (1991) model, and (b) the large field of view experimental data of Wang *et al.* (2020). The solid grey lines mark the location of $\lambda = 3l_0$.

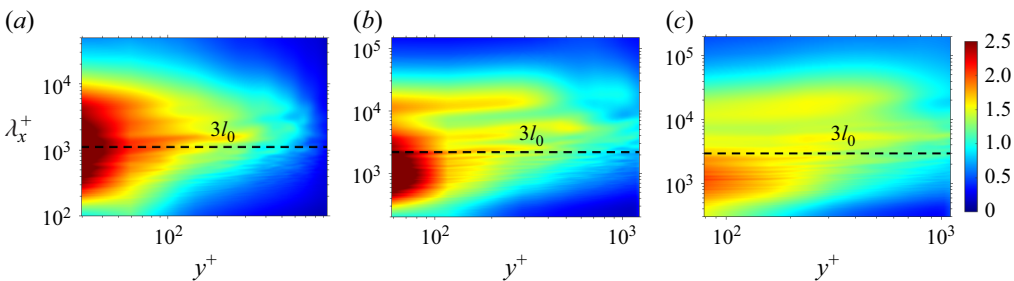


Figure 24. Premultiplied energy spectra, $k_x E_{u'u'}^+$, for the full turbulence at (a) $Re_\tau = 3300$, (b) $Re_\tau = 6700$ and (c) $Re_\tau = 8900$. The horizontal dashed lines correspond to $\lambda = 3l_0$, the characteristic wavelength of the compliant wall deformation.

in the streamwise velocity spectra (Perry & Chong 1982; Nickels *et al.* 2005; Calaf *et al.* 2013), are consistent with the so-called ‘attached eddies’ introduced by Townsend (1976). As demonstrated by Mathis *et al.* (2009), these eddies have a dominant peak in the buffer layer at $\lambda_x^+ \approx 1000$ in the premultiplied streamwise velocity spectra, $k_x E_{uu}$. The peak response of the compliant wall to harmonic excitation, based on a solution to the Helmholtz equation (Chase 1991; Zhang *et al.* 2017; Benschop *et al.* 2019; Wang *et al.* 2020), for a broad range of frequencies, is approximately three times the compliant layer thickness ($3l_0$), as long as the flow velocity and wave speed are lower than C_t , as demonstrated in figure 23(a). This preferred wavelength has been confirmed experimentally for several material properties and wall thicknesses by Zhang *et al.* (2017), Wang *et al.* (2020), Greidanus *et al.* (2022) and Lu *et al.* (2024). It should be noted that since the wave propagates at a speed scaled with U_0 , with coefficients varying between 0.4–0.8 (Carpenter *et al.* 2000), each frequency involves a different wavelength. Focusing on the frequency of peak material response, figure 23(b) provides sample experimental wavenumber spectra extracted from the Wang *et al.* (2020) results demonstrating that the peak wavelength is $3l_0$.

Figure 24 compares the energy spectra of the streamwise velocity fluctuations at the three Reynolds numbers premultiplied by k_x to emphasize the k^{-1} region, which represent the energetic attached eddies. Since the wavenumber range of the TPTV field of view is limited, these spectra are calculated in the frequency domain and converted to wavelength using Taylor’s frozen turbulence hypothesis. The peaks in all the premultiplied energy

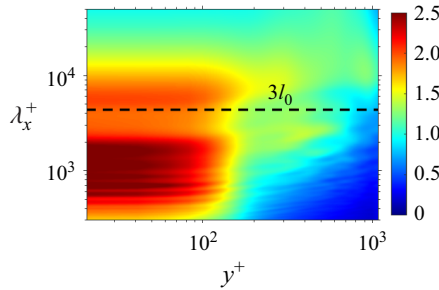


Figure 25. Contours of $k_x E_{u'u'}^+$ calculated from the Zhang *et al.* (2017) data at $Re_\tau = 2300$. The horizontal dashed line corresponds to $\lambda = 3l_0$.

spectra are centred around $\lambda_x^+ \approx 1000$, consistent with the findings in typical boundary layers over a wide range of Reynolds numbers (Mathis *et al.* 2009). However, the present data does not show their secondary peak at the wavelength of $\lambda_x \approx 10\delta$ for large-scale motions, possibly since the present recording time is only approximately $130\delta/U_0$. The black dashed lines mark the preferred deformation wavelength, $3l_0$. As is evident, at $Re_\tau = 3300$, the dominant deformation wavelength is well aligned with the peak of the premultiplied energy spectrum, indicating that the wall waves excite the flow at the preferred wavelength of the attached eddies. In contrast, the preferred surface wavelength falls at the edge of the k^{-1} range at the two higher Reynolds numbers, suggesting that it would cause weaker response and lower correlations with the flow. These observations are consistent with the decrease in all the coherent flow and stress parameters, as well as the decrease in flow–deformation correlations and coherence at the higher Reynolds numbers in spite of the substantially larger deformations. Additional evidence is provided by the comparison with the Zhang *et al.* (2017) results, for which the wall thickness, hence the preferred wavelength, is 3.2 times larger. In that case, the p' – d correlations are low (figure 22a) despite the near agreement in the magnitudes of d_{rms}^+ at $Re_\tau = 2300$ with those of the present values. The corresponding premultiplied spectrum calculated from that data, which is presented in figure 25, shows that the larger deformation wavelength deviates significantly from that of the energy-containing eddies. Hence, one should not be surprised by the low pressure–deformation correlations. Interestingly, in the Zhang *et al.* (2017) data, the mean flow hardly responds to the wall deformation, resulting in one-way flow–deformation coupling. In contrast, there are clear (but small) changes to the boundary layer mean velocity profile in the Wang *et al.* (2020) data at a similar Re_τ and d_{rms}^+ , but with a wall thickness matching the present values, suggesting that the boundary layer is more ‘sensitive’ to wall deformation.

It should be noted that in addition to the main peaks, the premultiplied spectra in figure 24 contain several lobes with a wide range of scales. Similar lobes have been seen in other experiments involving smooth rigid wall boundary layers and pipe flow (e.g. Guala, Hommema & Adrian 2006; Mathis *et al.* 2009), but have not received significant attention. In order to determine whether the present spectral undulations are associated with the deformation, figure 26(a–c) displays distribution of $k_x E_{uu}$ after subtracting the wave-coherent motions, leaving only stochastic part of the turbulence. While still visible, some of the lobes, e.g. those near $\lambda_x = 3l_0$ in all the three spectra, and those at $\lambda_x^+ > 10\,000$ at the two higher Reynolds numbers, have significantly lower magnitude, indicating that at least part of the energy in the lobes is associated with the wave-coherent motions, as is also demonstrated in the distribution of $k_x E_{\tilde{u}\tilde{u}}$ in figure 26(d–f). While the coherent energy at the lowest Reynolds number is broad and extends to the entire range of energy-containing

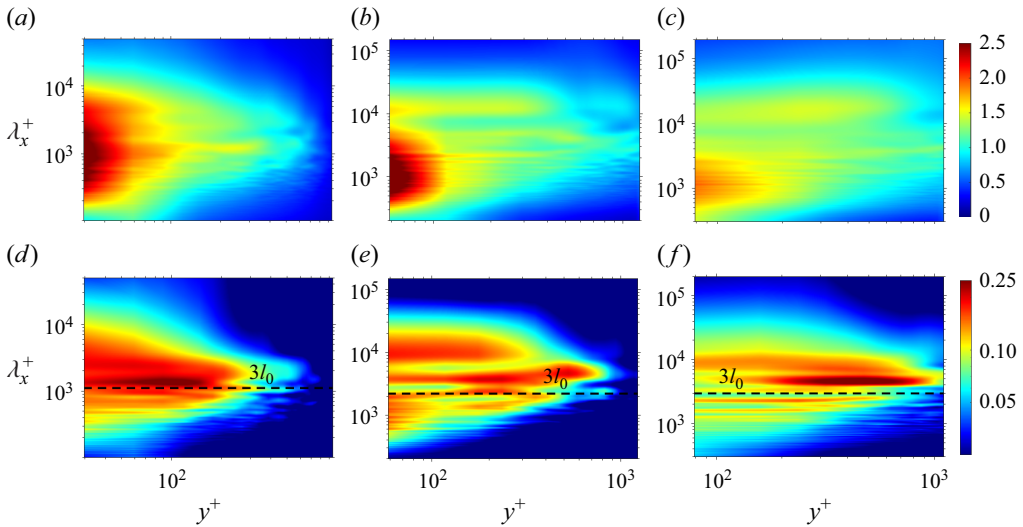


Figure 26. Contours of (a,b,c) $k_x E_{u''u''}^+$, and (d,e,f) $k_x E_{\tilde{u}\tilde{u}}^+$ at (a,d) $Re_\tau = 3300$, (b,e) $Re_\tau = 6700$ and (c,f) $Re_\tau = 8900$.

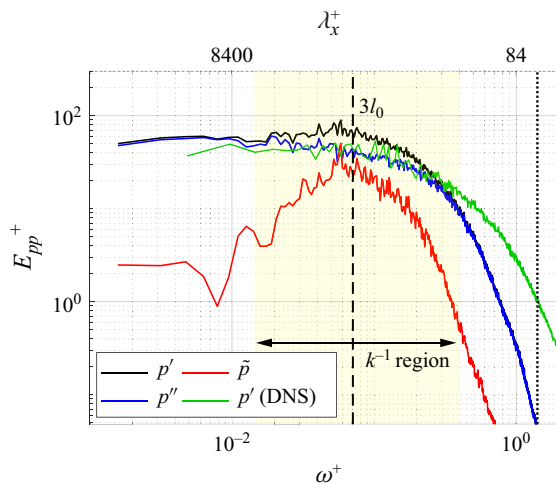


Figure 27. A comparison of the temporal spectra of the present total, wave-coherent and stochastic pressures at $y^+ = 30$ and $Re_\tau = 3300$ with the DNS channel flow pressure spectra at the same height and $Re_\tau = 1000$. The yellow background marks the k^{-1} region in the kinetic energy spectra, and the dotted line shows the experimental Nyquist frequency.

eddies, the results at the higher Reynolds numbers are patchy and extend well beyond the critical height, consistent with the distributions of the horizontal velocity fluctuation.

The next discussion examines the spectral content of the coherent and stochastic pressures. Figure 27 compares the total pressure spectrum at $y^+ = 30$ for $Re_\tau = 3300$, with those of the coherent and stochastic pressures. Also included is the pressure spectrum at the same elevation obtained from the Johns Hopkins Turbulence Database (Li *et al.* 2008; Graham *et al.* 2016) DNS for a rigid wall channel flow at $Re_\tau = 1000$. The Nyquist frequency of the experimental pressure spectra at $\omega^+ = 1.4$ is also marked. As is evident from figure 27, the present stochastic pressure spectra collapse well with the DNS spectra

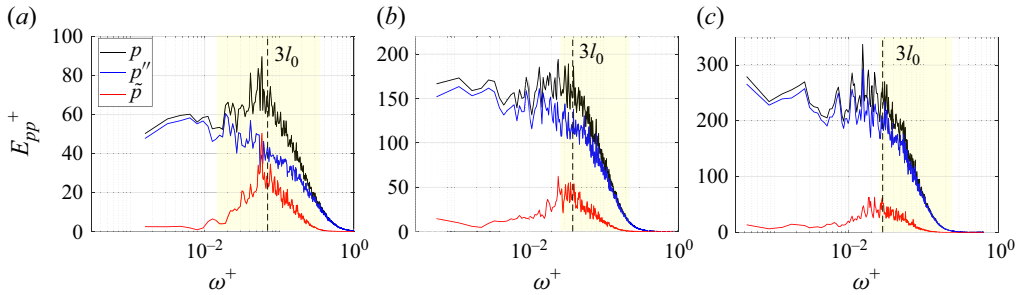


Figure 28. Temporal spectra of the total, coherent and stochastic pressures at (a) $Re_\tau = 3300$, (b) $Re_\tau = 6700$ and (c) $Re_\tau = 8900$.

at $\omega^+ < 0.4$ but deviate at higher frequencies. As shown in Agarwal *et al.* (2021), where the present particle tracking based pressure calculation method is introduced and calibrated, the calculated pressure deviates from the DNS data at frequencies exceeding 20 % of the Nyquist frequency, consistent with the trends depicted by the present results. The area highlighted by a yellow background corresponds to frequencies where the value of the k^{-1} premultiplied spectrum in figure 24(a) is higher than 75 % of its maximum value. The choice to use 75 % of the peak value as a threshold for defining the frequency bandwidth of the peak has been selected arbitrarily for illustration purpose, and is not used in any other analysis. Within this range, the present stochastic and DNS pressure spectra collapse, but the total pressure amplitude is clearly higher, especially in the vicinity of $3l_0$. The difference is associated with the peak in the coherent pressure in the same wavenumber range. In fact, around the peak, the coherent pressure amplitude is nearly equal to that of the stochastic level. Considering that the coherent pressure spectral peak fall in the energetic attached eddy range suggests that the flow and wall deformation are ‘resonating’. Figure 28 is a comparison between trends of the pressure spectra at the three Reynolds numbers, this time in a linear amplitude scale to highlight differences. These pressure spectra are sampled at $y/\delta = 0.009$, i.e. at the same distance from the wall as in figure 27. While the peak $E_{\tilde{p}\tilde{p}}$ at $Re_\tau = 3300$ is comparable to $E_{p''p''}$ in the energetic eddy range, $E_{p''p''}$ has a maximum at a significantly lower wavelength, demonstrating that the overall peak is attributable to $E_{\tilde{p}\tilde{p}}$. In contrast, the relative contributions of $E_{\tilde{p}\tilde{p}}$ at the higher Reynolds numbers are clearly much lower than the stochastic levels. We believe that these findings explain how submicron deformations at a frequency matching that of the energetic eddies in the boundary layer can cause more flow–deformation coupling than orders of magnitude higher deformations with mismatched frequencies.

5. Summary and conclusions

The interactions between high Reynolds number boundary layers with a compliant wall are investigated experimentally using simultaneous time-resolved TPTV to measure the 3-D flow and pressure field, and MZI to map the 2-D distribution of surface deformation. The present analysis extends the preliminary results described in Lu *et al.* (2024), in which we demonstrate the important role of the critical layer, where the local mean flow speed is equal to the surface wave speed. For the present compliant wall, the critical height increases from $60\delta_v$ at $Re_\tau = 3300$, to $190\delta_v$ at $Re_\tau = 8900$. Below the critical height, the turbulence is preferentially advected at the wave speed, while above it, the advection speed is equal to the local mean velocity. Furthermore, the coherence and correlation of flow parameters with the wall deformation peak at or near the critical height. However, both

the flow–deformation correlations and the coherence decrease with increasing Reynolds number in spite of the order of magnitude increase in deformation height. To explain this puzzling trend, in the present study, a Hilbert projection method is used for decomposing the velocity and pressure fluctuations to wave-coherent motions that are highly correlated with the surface waves, and stochastic turbulence that has a low correlation with the wall motion. The structure and trends of the two unsteady fields are then investigated separately, including the phase-averaged flows and pressures, Reynolds stresses, r.m.s. pressures, vorticity distributions as well as kinetic energies and their production rates.

The spatial distributions of phase-averaged coherent and stochastic flow variables reveal that all the wave-coherent flow variables have wave-phase dependent distributions. While all the coherent variables have high correlations with the surface wave, the correlation with the pressure is particularly high, peaking at 98 %. A negative spanwise vortex generates the pressure minimum at the deformation crest and a sweep-ejection transition is preferentially associated with pressure maximum at the trough. The negative vorticity peak aligned with the crest and the positive vorticity aligned with the trough are centred above the critical height. However, interaction of these vortices with the wall generates counter rotating vorticity below the critical layer. The coherent Reynolds stresses and pressure r.m.s. are an order of magnitude smaller than their stochastic counterparts, except for the pressure r.m.s. very near the wall, where the wave-coherent and stochastic values are comparable. Decomposition of the kinetic energy budget shows that both the wave-coherent and stochastic energy production rates are focused near the wall, well below the critical height, and that the former is 6 %–10 % of the latter, i.e. the mean flow transfer energy predominantly to the stochastic turbulence. The exchange between coherent and stochastic kinetic energies changes sign across the critical layer, flowing from the stochastic to the wave-coherent energy above the critical layer, and from the wave-coherent to the stochastic energy below the critical height. The coherent pressure diffusion term is negative around the peak of coherent energy above the critical layer, and positive below it. Finally, all the coherent flow variables and their correlations with the wave, from the phase-averaged velocity and pressure, to the Reynolds stresses and pressure r.m.s. and to the kinetic energy and transport terms, decrease with increasing Reynolds number, in contrast to the trends of the deformation amplitude.

To explain the strong flow–deformation interactions at the lowest Reynolds number, despite the submicron deformation height, we compare the characteristic deformation wavelength, three times the wall thickness, with the scales of the energy-containing attached eddies dominating the k^{-1} range of the turbulent energy spectrum. For this case, the deformation wavelength falls in the middle of the premultiplied streamwise energy spectrum ($k_x E_{uu}$), suggesting that the compliant wall waves resonate with the attached eddies. Indeed, $k_x E_{uu}$ contains lobes, some of them centred around the preferred surface wavelength, which contain significant wave-coherent energy. At higher Reynolds numbers, the deformation wavelength falls at the edge of the attached eddy range, as the deformation wavelength remains the same while these eddies decrease in size. Hence, the interactions become weaker even for considerably higher deformation amplitudes. Furthermore, when the scales overlap at the lowest Reynolds number, the near-wall coherent pressure spectrum at a wavelength corresponding to the surface wave is comparable in magnitude to the stochastic pressure, causing a significant increase in the overall pressure fluctuations. At higher Reynolds number, the coherent pressure is significantly smaller than the stochastic pressure spectra, which peak at other frequencies. These findings provide a plausible explanation on how turbulent eddies in a boundary layer become phase locked with submicron compliant wall deformations. They could guide the choice of compliant wall thickness that would maximize (or minimize) the wall-flow interactions in future efforts

aimed at developing flow control strategies. Future experiments should also focus on the flow–deformation interactions below the critical layer, hence require a higher resolution, and include means to determine the horizontal and vertical velocity fields of the compliant material.

One should keep in mind that the present deformation r.m.s. values are still smaller than δ_v . The flow–deformation interactions are expected to change significantly with further decrease in $E/\rho U_0^2$ and the resulting increase in deformation amplitude (Wang *et al.* 2020; Greidanus *et al.* 2022). For example, flow separation might occur at the crest of the deformation (Esteghamatian *et al.* 2022), and surface instabilities, e.g. static-divergence waves, might develop when the flow speed exceeds the material shear speed (Gad-El-Hak *et al.* 1984; Duncan 1986; Greidanus *et al.* 2022).

Funding. This project is funded by the Office of Naval Research under grant numbers N00014-23-1-2681 and N00014-20-1-2778. Greg Orris, Christine Sanders, and Meredith Hutchinson are the programme officers. The authors would also like to thank the late Y. Ronzhes for designing the water tunnel.

Declaration of interests. The authors report no conflict of interest.

Appendix A. The Hilbert projection method

For a real-valued deformation, $d(x, z, t)$, the Hilbert transform (see comprehensive tutorials in Bendat & Piersol 1986), denoted as $\mathcal{D}(t)$, is given by

$$\mathcal{D}(t) = \mathcal{H}\{d(t)\} = \frac{1}{\pi} p.v. \int_{-\infty}^{+\infty} \frac{d(\tau)}{t - \tau} d\tau, \quad (\text{A1})$$

where \mathcal{H} indicates the Hilbert transform operator, *p.v.* represents the Cauchy principal value of the integral and τ is a time shift. Equivalently, $\mathcal{D}(t)$ is the convolution (denoted by $*$) of $d(t)$ with $(1/\pi t)$,

$$\mathcal{D}(t) = d(t) * (1/\pi t). \quad (\text{A2})$$

The Fourier transform of $\mathcal{D}(t)$ is given by

$$\mathcal{F}\{\mathcal{D}(t)\} = \mathcal{F}\{d(t)\} \cdot \mathcal{F}\left\{\frac{1}{\pi t}\right\} = \hat{d}(\omega) \cdot \{-i \operatorname{sgn}(\omega)\} = \begin{cases} i\hat{d}(\omega) & \text{for } \omega < 0, \\ 0 & \text{for } \omega = 0, \\ -i\hat{d}(\omega) & \text{for } \omega > 0, \end{cases} \quad (\text{A3})$$

where $\hat{d}(\omega)$ is the Fourier transform of $d(t)$. Hence, $\mathcal{D}(t)$ can be readily calculated from the inverse Fourier transform of (A3). The functions $d(t)$ and $\mathcal{D}(t)$ form a quadrature pair, i.e. they have a phase difference of $\pi/2$, defining the following complex analytic form:

$$\psi(t) = d(t) + i\mathcal{D}(t) = A(t)e^{i\phi(t)}, \quad (\text{A4})$$

where $A(t) = \sqrt{d(t)^2 + \mathcal{D}(t)^2}$ and $\phi(t) = \tan^{-1}\{\mathcal{D}(t)/d(t)\}$ are the amplitude and phase of $\psi(t)$, respectively.

Following Hristov *et al.* (1998), the Hilbert projection method consists of the following steps. First, the original $d(t)$ signal is divided into a series of narrow bandpass filtered signals denoted as $d_k(t)$ in the frequency domain, each with a bandwidth of $\Delta\omega = 0.15U_0/l_0$. Using the Fourier modes of $d(t)$,

$$d_k(t) = \sum_{\omega_k - \Delta\omega/2 < \omega_n < \omega_k + \Delta\omega/2} C_n e^{i(\omega_n t)}, \quad (\text{A5})$$

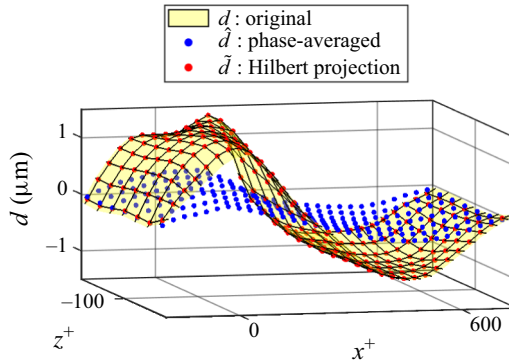


Figure 29. Sample instantaneous snapshots of the original, phase-averaged and Hilbert-projected deformations. The presented region is for $x^+ = -200 \sim 750$, $z^+ = -200 \sim 0$ at $Re_\tau = 3300$.

where the Fourier coefficients, C_n , are obtained using fast Fourier transform in MATLAB. For each $d_k(t)$, we construct its analytic signal $\psi_k(t)$, similar to equation (A4). The wave coherent part of a signal, \tilde{f} , is obtained by projecting f' onto $\psi_k(t)$, namely

$$\tilde{f} = Real \left\{ \sum_k \frac{\langle f', \psi_k \rangle}{\|\psi_k\|^2} \psi_k \right\}, \quad (A6)$$

where $\langle \cdot \rangle$ indicates an inner product, and $\|\cdot\|^2$ is the squared norm. In Hristov & Plancarte (2014) and Wu, Hristov & Rutgersson (2018), (A6) is further clarified to indicate that

$$\tilde{f} = \sum_k \left\{ \frac{\langle f', d_k \rangle}{\|d_k\|^2} d_k + \frac{\langle f', \mathcal{D}_k \rangle}{\|\mathcal{D}_k\|^2} \mathcal{D}_k \right\}. \quad (A7)$$

Since d_k and \mathcal{D}_k have a phase difference of $\pi/2$, the ratio of these projections gives the phase lag between \tilde{f} and d_k .

To demonstrate the advantage of the Hilbert projection method introduced by Hristov *et al.* (1998), we first examine its ability to reproduce the original wave, i.e. the wave-coherent deformation should be nearly equal to the deformation itself, $\tilde{d}(x, z, t) \sim d(x, z, t)$. Subsequently, correlations are used for confirming the high coherence between the deformation and projected flow variables, such as pressure and velocity. As a baseline for comparison, the projection results are compared with the phase-averaged deformation and flow variables, denoted as $\hat{d}(x, z, t)$ and $\hat{f}(x, z, t)$. The latter are evaluated using the following steps. For each snapshot, an instantaneous phase is assigned to each (x, z) point based on the Hilbert Transform of $d(x, z, t)$. Based on the definitions above, phases 0 and $\pm\pi$ are assigned to the wave crest and trough, respectively. The interval between peaks is divided to 20 bins, each with a phase width of $\pi/10$, and record the location and flow variables corresponding to each bin. Results obtained for the entire data set are then phase-averaged to obtain \hat{d} and \hat{f} . In addition, figure 29 compares a sample snapshot of $d(x, z, t)$ at $Re_\tau = 3300$, with the instantaneous $\tilde{d}(x, z, t)$ and $\hat{d}(\phi)$, where the instantaneous phase of the peak in $d(x, z, t)$ is matched with $\phi = 0$ of the phase-averaged waveform. As is evident, $\tilde{d}(x, z, t)$ reproduces $d(x, z, t)$, and in fact, the temporal correlation between them for the entire data is 99.9 %. In contrast, the temporal correlation of \hat{d} with the original signal is 78 %. Figure 30 compares the coherent pressure and vertical velocity component with the phase-averaged distributions. The maximum temporal $\tilde{p}-d$ and $\tilde{v}-d$ correlations, obtained after shifting the time series relative to each other and finding the maximum values, are 96 % and 75 %, respectively.

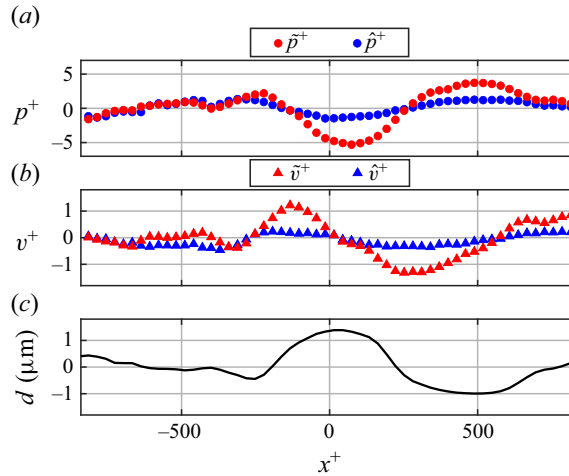


Figure 30. Sample instantaneous distributions of (a) \tilde{p} and \hat{p} , (b) \tilde{v} and \hat{v} , (c) d at $z^+ = -100$ and $Re_\tau = 3300$.

respectively. The corresponding maximum \hat{p} - d and \hat{v} - d correlations are only 76 % and 58 %. Clearly, the Hilbert projection is an effective tool for finding the coherent part of the signal. The remaining incoherent part of the pressure or flow variables, which are referred to as ‘stochastic’ are obtained by subtracting the coherent signal from the original data.

REFERENCES

- ADRIAN, R.J. 2007 Hairpin vortex organization in wall turbulence. *Phys. Fluids* **19** (4), 041301.
- AGARWAL, K., RAM, O., LU, Y. & KATZ, J. 2023 On the pressure field, nuclei dynamics and their relation to cavitation inception in a turbulent shear layer. *J. Fluid Mech.* **966**, A31.
- AGARWAL, K., RAM, O., WANG, J., LU, Y. & KATZ, J. 2021 Reconstructing velocity and pressure from noisy sparse particle tracks using constrained cost minimization. *Exp. Fluids* **62**, 1–20.
- BAI, K. & KATZ, J. 2014 On the refractive index of sodium iodide solutions for index matching in PIV. *Exp. Fluids* **55**, 1–6.
- BENDAT, J.S. & PIERSON, A.G. 1986 *Random Data: Analysis and Measurement Procedure*. 2nd edn. Wiley InterScience.
- BENJAMIN, T.B. 1960 Effects of a flexible boundary on hydrodynamic stability. *J. Fluid Mech.* **9**, 513–532.
- BENSCHOP, H.O.G., GREIDANUS, A.J., DELFOS, R., WESTERWEE, J. & BREUGEM, W.-P. 2019 Deformation of a linear viscoelastic compliant coating in a turbulent flow. *J. Fluid Mech.* **859**, 613–658.
- BOGGS, F.W. & HAHN, E.R. 1962 Performance of compliant skins in contact with high velocity flow in water. In *Proc. 7th Joint Army-Navy-Air Force Conf. on Elastomer Research and Development*, vol. 2, pp.443. Office of Naval Research.
- BUCKLEY, M.P. & VERON, F. 2019 The turbulent airflow over wind generated surface waves. *Eur. J. Mech. (B/Fluids)* **73**, 132–143.
- BUSSE, A. & JELLY, T.O. 2023 Effect of high skewness and kurtosis on turbulent channel flow over irregular rough walls. *J. Turbul.* **24** (1–2), 57–81.
- CALAF, M., HULTMARK, M., OLDROYD, H.J., SIMEONOV, V. & PARLANGE, M.B. 2013 Coherent structures and the k^{-1} spectral behaviour. *Phys. Fluids* **25** (12), 125107.
- CAO, T. & SHEN, L. 2021 A numerical and theoretical study of wind over fast-propagating water waves. *J. Fluid Mech.* **919**, A38.
- CARPENTER, J.R., BUCKLEY, M.P. & VERON, F. 2022 Evidence of the critical layer mechanism in growing wind waves. *J. Fluid Mech.* **948**, A26.
- CARPENTER, P.W., DAVIES, C. & LUCEY, A.D. 2000 Hydrodynamics and compliant walls: does the dolphin have a secret? *J. Curr. Sci.* **79**, 758–765.
- CASTELLINI, P., MARTARELLI, M. & TOMASINI, E.P. 2006 Laser doppler vibrometry: development of advanced solutions answering to technology’s needs. *Mech. Syst. Signal Process.* **20**, 1265–1285.

- CHARRUAULT, F., GREIDANUS, A.J., BREUGEM, W.-P. & WESTERWEEL, J. 2018 A dot tracking algorithm to measure free surface deformations. In *Proceedings 18th International Symposium on Flow Visualization*. Eth Zurich.
- CHASE, D.M. 1991 Generation of fluctuating normal stress in a viscoelastic layer by surface shear stress and pressure as in turbulent boundary-layer flow. *J. Acoust. Soc. Am.* **89** (6), 2589–2596.
- CHOI, K.-S., YANG, X., CLAYTON, B.R., GLOVER, E.J., ATLAR, M., SEMENOV, B.N. & KULIK, V.M. 1997 Turbulent drag reduction using compliant surfaces. *Proc. R. Soc. Lond. A.* **453** (1965), 2229–2240.
- DE GRAAFF, D.B. & EATON, J.K. 2000 Reynolds-number scaling of the flat-plate turbulent boundary layer. *J. Fluid Mech.* **422**, 319–346.
- DO, J., WANG, B. & CHANG, K.A. 2024 Turbulence over young wind waves dominated by capillaries and micro-breakers. *J. Fluid Mech.* **985**, A22.
- DUNCAN, J.H. 1986 The response of an incompressible viscoelastic coating to pressure fluctuations in a turbulent boundary layer. *J. Fluid Mech.* **171**, 339–363.
- EINAUDI, F. & FINNIGAN, J. 1993 Wave-turbulence dynamics in the stably stratified boundary layer. *J. Atmos. Sci.* **50** (13), 1841–1864.
- ENDO, T. & HIMENO, R. 2002 Direct numerical simulation of turbulent flow over a compliant surface. *J. Turbul.* **3** (1), 7.
- ESTEGHAMATIAN, A., KATZ, J. & ZAKI, T.A. 2022 Spatiotemporal characterization of turbulent channel flow with a hyperelastic compliant wall. *J. Fluid Mech.* **942**, A35.
- FERNHOLZ, H.H. & FINLEY, P.J. 1996 The incompressible zero-pressure-gradient turbulent boundary layer – an assessment of the data. *Prog. Aero. Sci.* **32**, 245–311.
- FISHER, D.H. & BLICK, E.F. 1966 Turbulent damping by flabby skins. *J. Aircraft.* **3** (2), 163–164.
- FLACK, K.A. & SCHULTZ, M.P. 2014 Roughness effects on wall-bounded turbulent flows. *Phys. Fluids* **26** (10), 101305.
- FREUND, L.B. 1998 *Dynamic Fracture Mechanics*. Cambridge University Press.
- FUKAGATA, K., KERN, S., CHATELAIN, P., KOUMOUTSAKOS, P. & KASAGI, N. 2008 Evolutionary optimization of an anisotropic compliant surface for turbulent friction drag reduction. *J. Turbul.* **9**, N35.
- GAD-EL-HAK, M. 1986 The response of elastic and viscoelastic surfaces to a turbulent boundary layer. *Trans. ASME E: J. Appl. Mech.* **53**, 206–212.
- GAD-EL-HAK, M., BLACKWELDER, R.F. & RILEY, J.J. 1984 On the interaction of compliant coatings with boundary-layer flows. *J. Fluid Mech.* **140**, 257–280.
- GANAPATHISUBRAMANI, B., HUTCHINS, N., HAMBLETON, W.T., LONGMIRE, E.K. & MARUSIC, I. 2005 Investigation of large-scale coherence in a turbulent boundary layer using two-point correlations. *J. Fluid Mech.* **524**, 57–80.
- GEORGE, W.K. & CASTILLO, L. 1997 Zero-pressure-gradient turbulent boundary layer. *Appl. Mech. Rev.* **50**, 689–729.
- GRAHAM, J., *et al.* 2016 A Web services accessible database of turbulent channel flow and its use for testing a new integral wall model for LES. *J. Turbul.* **17** (2), 181–215.
- GRARE, L., LENAIN, L. & MELVILLE, W.K. 2013 Wave-coherent airflow and critical layers over ocean waves. *J. Phys. Oceanogr.* **43** (10), 2156–2172.
- GREIDANUS, A.J., DELFOS, R., PICKEN, S.J. & WESTERWEEL, J. 2022 Response regimes in the fluid–structure interaction of wall turbulence over a compliant coating. *J. Fluid Mech.* **952**, A1.
- GUALA, M., HOMMEMA, S.E. & ADRIAN, R.J. 2006 Large-scale and very-large-scale motions in turbulent pipe flow. *J. Fluid Mech.* **554**, 521–542.
- HARA, T. & SULLIVAN, P.P. 2015 Wave boundary layer turbulence over surface waves in a strongly forced condition. *J. Phys. Oceanogr.* **45** (3), 868–883.
- HRISTOV, T.S. & RUIZ-PLANCARTE, J. 2014 Dynamic balances in a wavy boundary layer. *J. Phys. Oceanogr.* **44** (12), 3185–3194.
- HRISTOV, T.S., FRIEHE, C. & MILLER, S. 1998 Wave-coherent fields in air flow over ocean waves: identification of cooperative behavior buried in turbulence. *Phys. Rev. Lett.* **81** (23), 5245.
- HRISTOV, T.S., MILLER, S. & FRIEHE, C. 2003 Dynamical coupling of wind and ocean waves through wave-induced air flow. *Nature*. **422** (6927), 55–58.
- HSU, C.T., HSU, E.Y. & STREET, R.L. 1981 On the structure of turbulent flow over a progressive water wave: theory and experiment in a transformed, wave-following co-ordinate system. *J. Fluid Mech.* **105**, 87–117.
- HULTMARK, M., VALLIKIVI, M., BAILEY, S.C.C. & SMITS, A.J. 2012 Turbulent pipe flow at extreme Reynolds numbers. *Phys. Rev. Lett.* **108** (9), 094501.
- HUNT, J.C.R., LEBOVICH, S. & RICHARDS, K.J. 1988 Turbulent shear flows over low hills. *Q. J. R. Meteorol. Soc.* **114** (484), 1435–1470.
- HUSSAIN, A.K.M.F. & REYNOLDS, W.C. 1970 The mechanics of an organized wave in turbulent shear flow. *J. Fluid Mech.* **41** (2), 241–258.

- HUTCHINS, N. & MARUSIC, I. 2007 Evidence of very long meandering features in the logarithmic region of turbulent boundary layers. *J. Fluid Mech.* **579**, 1–28.
- HUYNH, D. & MCKEON, B. 2020 Measurements of a turbulent boundary layer-compliant surface system in response to targeted, dynamic roughness forcing. *Exp. Fluids* **61**, 1–15.
- JEFFREYS, H. 1925 On the formation of water waves by wind. *Proc. R. Soc. Lond. A*. **107**, 189–206.
- JEONG, J. & HUSSAIN, F. 1995 On the identification of a vortex. *J. Fluid Mech.* **285**, 69–94.
- JIMÉNEZ, J. 2018 Coherent structures in wall-bounded turbulence. *J. Fluid Mech.* **842**, P1.
- JIMÉNEZ, J., HOYAS, S., SIMENS, M.P. & MIZUNO, Y. 2010 Turbulent boundary layers and channels at moderate Reynolds numbers. *J. Fluid Mech.* **657**, 335–360.
- KRAMER, M.O. 1957 Boundary-layer stabilization by distributed damping. *J. Aero. Sci.* **24**, 459–460.
- KRAMER, M.O. 1962 Boundary-layer stabilization by distributed damping. *Naval Engrs J.* **74** (2), 341–348.
- KRASITSKII, V.P. & ZASLAVSKII, M.M. 1978 Comments on the Phillips’-Miles’ theory of wind wave generation. *Boundary-Layer Meteorol.* **14** (2), 199–215.
- KUMAR, P. & MAHESH, K. 2022 A method to determine wall shear stress from mean profiles in turbulent boundary layers. *Exp. Fluids* **63** (1), 6.
- LANDAHL, M.T. 1962 On the stability of a laminar incompressible boundary layer over a flexible surface. *J. Fluid Mech.* **13**, 609–632.
- LEE, M. & MOSER, R.D. 2015 Direct numerical simulation of turbulent channel flow up to $re_\tau \approx 5200$. *J. Fluid Mech.* **774**, 395–415.
- LEE, T., FISHER, M. & SCHWARZ, W.H. 1993a Investigation of the stable interaction of a passive compliant surface with a turbulent boundary layer. *J. Fluid Mech.* **257**, 373–401.
- LEE, T., FISHER, M. & SCHWARZ, W.H. 1993b The measurement of flow-induced surface displacement on a compliant surface by optical holographic interferometry. *Exp. Fluids* **14**, 159–168.
- LEE, T., FISHER, M. & SCHWARZ, W.H. 1995 Investigation of the effects of a compliant surface on boundary-layer stability. *J. Fluid Mech.* **288**, 37–58.
- LI, Y., PERLMAN, E., WAN, M., YANG, Y., MENEVEAU, C., BURNS, R., CHEN, S., SZALAY, A. & EYINK, G. 2008 A public turbulence database cluster and applications to study lagrangian evolution of velocity increments in turbulence. *J. Turbul.* **9**, N31.
- LIGHTHILL, M.J. 1963 Boundary layer theory. In *Laminar Boundary Layers*, (L. ROSENHEAD), pp. 46–103. Oxford University Press.
- LIGHTHILL, M.J. 1962 Physical interpretation of the mathematical theory of wave generation by wind. *J. Fluid Mech.* **14** (3), 385–398.
- LISSAMAN, P.B.S. & HARRIS, G.L. 1969 Turbulent skin friction on compliant surfaces. *AIAA J.* **7** (8), 1625–1627.
- LIU, X. & KATZ, J. 2006 Instantaneous pressure and material acceleration measurements using a four-exposure PIV system. *Exp. Fluids* **41**, 227–240.
- LU, Y., RAM, O., JOSE, J., AGARWAL, K. & KATZ, J. 2021 A water tunnel with inline cyclone separator for removing freestream bubble. In *Proceedings of the 11th International Symposium on Cavitation*. Available at: http://cav2021.org/wp-content/uploads/2021/07/P00125_optimize-3.pdf.
- LU, Y., XIANG, T., ZAKI, T.A. & KATZ, J. 2024 On the scaling and critical layer in a turbulent boundary layer over a compliant surface. *J. Fluid Mech.* **980**, R2.
- MAKIN, V.K. & KUDRYAVTSEV, V.N. 1999 Coupled sea surface–atmosphere model: 1. Wind over waves coupling. *J. Geophys. Res: Oceans* **104** (C4), 7613–7623.
- MATHIS, R., HUTCHINS, N. & MARUSIC, I. 2009 Large-scale amplitude modulation of the small-scale structures in turbulent boundary layers. *J. Fluid Mech.* **628**, 311–337.
- MCMICHAEL, J.M., KLEBANOFF, P.S. & MEASE, N.E. 1980 Experimental investigation of drag on a compliant surface. *Prog. Astronaut. Aeronaut.* **72**, 410–438.
- MEINHART, C.D., WERELEY, S.T. & SANTIAGO, J.G. 2000 A piv algorithm for estimating time-averaged velocity fields. *J. Fluids Engng* **122** (2), 285–289.
- MILES, J.W. 1957 On the generation of surface waves by shear flows. *J. Fluid Mech.* **3** (2), 185–204.
- MORRILL-WINTER, C., PHILIP, J. & KLEWICKI, J. 2017 An invariant representation of mean inertia: theoretical basis for a log law in turbulent boundary layers. *J. Fluid Mech.* **813**, 594–617.
- MORTON, B.R. 1984 The generation and decay of vorticity. *Geophys. Astrophys. Fluid Dyn.* **28** (3–4), 277–308.
- NAKATO, M., ONOGI, H., HIMENO, Y., TANAKA, I. & SUZUKI, T. 1985 Resistance due to surface roughness. In *Proceedings of the 15th Symposium on Naval Hydrodynamics*, pp. 553–568.
- NAPOLI, E., ARMENIO, V. & DE MARCHIS, M. 2008 The effect of the slope of irregularly distributed roughness elements on turbulent wall-bounded flows. *J. Fluid Mech.* **613**, 385–394.

- NICKELS, T.B., MARUSIC, I., HAFEZ, S. & CHONG, M.S. 2005 Evidence of the k_l^{-1} law in high-reynolds number turbulent boundary layer. *Phys. Rev. Lett.* **95**, 074501.
- PERRY, A.E. & CHONG, M.S. 1982 On the mechanism of wall turbulence. *J. Fluid Mech.* **119**, 173–217.
- PHILLIPS, O.M. 1957 On the generation of waves by turbulent wind. *J. Fluid Mech.* **2** (5), 417–445.
- POPE, S.B. 2000 *Turbulent Flows*. Cambridge University Press.
- RAFFEL, M., WILLERT, C.E., SCARANO, F., KÄHLER, C.J., WERELEY, S.T. & KOMPENHANS, J. 2018 *Particle Image Velocimetry: A Practical Guide*. 3rd edn. Springer.
- REYNOLDS, W.C. & HUSSAIN, A.K.M.F. 1972 The mechanics of an organized wave in turbulent shear flow. Part 3. Theoretical models and comparisons with experiments. *J. Fluid Mech.* **54** (2), 263–288.
- RILEY, D.S., DONELAN, M.A. & HUI, W.H. 1982 An extended Miles' theory for wave generation by wind. *Boundary-Layer Meteorol.* **22**, 209–225.
- ROSTI, M.E. & BRANDT, L. 2017 Numerical simulation of turbulent channel flow over a viscous hyper-elastic wall. *J. Fluid Mech.* **830**, 708–735.
- RUTGERSSON, A. & SULLIVAN, P.P. 2005 The effect of idealized water waves on the turbulence structure and kinetic energy budgets in the overlying airflow. *Dyn. Atmos. Oceans.* **38** (3–4), 147–171.
- SCHANZ, D., GESEMANN, S. & SCHRÖDER, A. 2016 Shake-The-Box: Lagrangian particle tracking at high particle image densities. *Exp. Fluids* **57**, 1–27.
- SCHULTZ, M.P. & FLACK, K.A. 2009 Turbulent boundary layers on a systematically varied rough wall. *Phys. Fluids* **21** (1), 015104.
- SCHULTZ, M.P. & FLACK, K.A. 2013 Reynolds-number scaling of turbulent channel flow. *Phys. Fluids* **25** (2), 025104.
- SILLERO, J.A., JIMÉNEZ, J. & MOSER, R.D. 2014 Two-point statistics for turbulent boundary layers and channels at Reynolds numbers up to $\delta^+ \approx 2000$. *Phys. Fluids* **26** (10), 105109.
- TOWNSEND, A.A. 1976 *the Structure of Turbulent Shear Flow*. 2nd edn. Cambridge University Press.
- WANG, J., KOLEY, S.S. & KATZ, J. 2020 On the interaction of a compliant wall with a turbulent boundary layer. *J. Fluid Mech.* **899**, A20.
- WANG, J., ZHANG, C. & KATZ, J. 2019 GPU-based, parallel-line, omni-directional integration of measured pressure gradient field to obtain the 3D pressure distribution. *Exp. Fluids* **60**, 1–24.
- WANG, Z., YEO, K.S. & KHOO, B.C. 2006 On two-dimensional linear waves in Blasius boundary layer over viscoelastic layers. *Eur. J. Mech. (B/Fluids)* **25** (1), 33–58.
- WEI, T., SCHMIDT, R. & MCMURTRY, P. 2005 Comment on the Clauser chart method for determining the friction velocity. *Exp. Fluids* **38**, 695–699.
- WU, L., HRISTOV, T. & RUTGERSSON, A. 2018 Vertical profiles of wave-coherent momentum flux and velocity variances in the marine atmospheric boundary layer. *J. Phys. Oceanogr.* **48** (3), 625–641.
- YANG, D. & SHEN, L. 2010 Direct-simulation-based study of turbulent flow over various waving boundaries. *J. Fluid Mech.* **650**, 131–180.
- YOUSEFI, K. & VERON, F. 2020 Boundary layer formulations in orthogonal curvilinear coordinates for flow over wind-generated surface waves. *J. Fluid Mech.* **888**, A11.
- YOUSEFI, K., VERON, F. & BUCKLEY, M.P. 2021 Turbulent and wave kinetic energy budgets in the airflow over wind generated surface waves. *J. Fluid Mech.* **920**, A33.
- ZHANG, C., MIORINI, R. & KATZ, J. 2015 Integrating Mach–Zehnder interferometry with TPIV to measure the time-resolved deformation of a compliant wall along with the 3D velocity field in a turbulent channel flow. *Exp. Fluids* **56** (11), 203.
- ZHANG, C., WANG, J., BLAKE, W. & KATZ, J. 2017 Deformation of a compliant wall in a turbulent channel flow. *J. Fluid Mech.* **823**, 345–390.
- ZHANG, E., WANG, Z. & LIU, Q. 2024 A numerical investigation of momentum flux and kinetic energy transfers between turbulent wind and propagating waves. *Flow* **4**, E14.